



## Full Length Article

## Indentation-induced deformation twinning in magnesium: Phase-field modeling of microstructure evolution and size effects

Mohsen Rezaee-Hajidehi, Przemysław Sadowski, Stanisław Stupkiewicz\*

*Institute of Fundamental Technological Research (IPPT), Polish Academy of Sciences, Pawińskiego 5B, 02-106 Warsaw, Poland*

Received 25 November 2024; received in revised form 29 January 2025; accepted 18 February 2025

Available online 9 April 2025

**Abstract**

Magnesium is distinguished by its highly anisotropic inelastic deformation involving a profuse activity of deformation twinning. Instrumented micro/nano-indentation technique has been widely applied to characterize the mechanical properties of magnesium, typically through the analysis of the indentation load–depth response, surface topography, and less commonly, the post-mortem microstructure within the bulk material. However, experimental limitations prevent the real-time observation of the evolving microstructure. To bridge this gap, we employ a recently-developed finite-strain model that couples the phase-field method and conventional crystal plasticity to simulate the evolution of the indentation-induced twin microstructure and its interaction with plastic slip in a magnesium single-crystal. Particular emphasis is placed on two aspects: orientation-dependent inelastic deformation and indentation size effects. Several outcomes of our 2D computational study are consistent with prior experimental observations. Chief among them is the intricate morphology of twin microstructure obtained at large spatial scales, which, to our knowledge, represents a level of detail that has not been captured in previous modeling studies. To further elucidate on size effects, we extend the model by incorporating gradient-enhanced crystal plasticity, and re-examine the notion of ‘smaller is stronger’. The corresponding results underscore the dominant influence of gradient plasticity over the interfacial energy of twin boundaries in governing the size-dependent mechanical response.

© 2025 Chongqing University. Publishing services provided by Elsevier B.V. on behalf of KeAi Communications Co. Ltd.

This is an open access article under the CC BY license (<http://creativecommons.org/licenses/by/4.0/>)

Peer review under responsibility of Chongqing University

**Keywords:** Magnesium alloys; Deformation twinning; Micro/nano-indentation; Microstructure evolution; Phase-field method; Crystal plasticity.**1. Introduction**

Inelastic deformation in magnesium and its alloys proceeds predominantly through the activation and interaction of dislocation slip and deformation twinning. In magnesium, with a low-symmetry hexagonal close-packed (HCP) crystal structure, dislocation slip occurs on crystallographic planes and along crystallographic directions with varying atomic packing densities. As a result, the activation barrier, i.e., the critical resolved shear stress (CRSS), differs significantly between basal and non-basal slip systems [1,2]. At room temperature, due to the high CRSS required to activate non-basal slip systems, deformation twinning, and in particular the  $\{10\bar{1}2\}\{1011\}$  ten-

sile twinning, emerges as a dominant inelastic mechanism to accommodate strains along the  $c$ -axis of the HCP lattice. It thus compensates for the scarcity of easily-activated non-basal slip systems [3–5]. Twinning is characterized by a constant shear, imposes an abrupt lattice reorientation of about  $86^\circ$ , and possesses a polar nature, that is, its activation depends on the shear direction within the twin plane. Collectively, the aforementioned factors give rise to a highly anisotropic inelastic deformation in magnesium. As such, predictive modeling of the underlying microstructure can play a pivotal role in understanding the mechanical behavior of magnesium, and it forms the main objective of this work.

Instrumented micro/nano-indentation technique has been extensively applied to single- and poly-crystalline magnesium to identify the primary inelastic contributors to deformation, probe their inherent characteristics, and thereby, gain deeper insights into the macroscopic mechanical behavior. Several

\* Corresponding author.

E-mail addresses: [mrezaee@ippt.pan.pl](mailto:mrezaee@ippt.pan.pl) (M. Rezaee-Hajidehi), [psad@ippt.pan.pl](mailto:psad@ippt.pan.pl) (P. Sadowski), [sstupkie@ippt.pan.pl](mailto:sstupkie@ippt.pan.pl) (S. Stupkiewicz).

key observations have been drawn from numerous indentation studies on magnesium alloys. (i) At small scales, the initial yielding is often accompanied by an abrupt displacement burst, known as pop-in, in the indentation load–depth response. Pop-ins not only mark the onset of dislocation glide but also the twin nucleation, e.g., [6–8]. Interestingly, pop-ins have been also detected during indentation unloading and have been attributed to detwinning, i.e., the retraction of twin boundaries [9]. (ii) Magnesium alloys exhibit a strong orientation-dependent behavior. The load–depth response, the pop-ins, the morphology of the indent, and the active slip systems and twin variants are all strongly influenced by the crystallographic orientation on which the indentation is performed, e.g., [10–14]. Notably, indentation perpendicular to the *c*-axis is most favorable for the activation of tensile twins. (iii) In addition to the well-documented size effects associated with dislocation mobility, twinning is also subject to strong size effects. The contribution of twinning to deformation has been shown to diminish with decreasing indentation depth, indenter radius and grain size, e.g., [11,13–16].

Combining instrumented indentation with advanced imaging and visualization techniques provides valuable information about the indentation-induced microstructure, which complements the measured load–depth response and facilitates the identification of active inelastic mechanisms. Unlike uniaxial tension/compression tests, indentation generates a complex stress state beneath the indenter, leading to intricate microstructural changes driven by the intertwined action of multiple mechanisms [11]. This complexity underscores the importance of combining instrumented indentation with imaging techniques for a more comprehensive analysis. Imaging can be performed during the indentation test to track the topographical changes near the indent surface, or afterward to examine the residual imprint or the microstructural changes deep inside the bulk material. For instance, using optical microscopy and electron backscatter diffraction (EBSD) analysis, Kitahara et al. [17] delivered unprecedented visualization of the remnant twin microstructure within cross-sectional cuts of indented magnesium. The observed microstructure, as depicted in Fig. 1, revealed important details, including the overall microstructural pattern, the participating twin variants, and the characteristic lenticular morphology of the individual twins.

Despite the valuable insights gleaned from in-situ and ex-situ analyses, there remains ambiguity concerning how the microstructure evolves beneath the indenter. Indeed, a thorough understanding of phenomena such as pop-ins, orientation-dependent behavior, and size effects hinges on linking macroscopic observations with underlying microstructural events, which is only feasible when real-time data on the evolution of twinning/detwinning and dislocation slip is available. Moreover, it is important to acknowledge that microstructural changes may arise during the indentation unloading [9,18,19], as well as during the subsequent cross-sectional cutting process. Consequently, the extracted microstructure may not fully represent the state of the material at the end of the loading stage. One possible approach to overcome this constraint is to

employ geometries with a sufficiently large field of view, such as micro/nano-pillars, which allow for a transparent tracking of the microstructure on free surfaces. However, in view of the strong influence of pre-existing defects and the presence of free surfaces, the nucleation stresses measured in these experiments deviate significantly from those in indentation experiments and from theoretical predictions [19–21]. This discrepancy rules out the possibility of inferring the indentation-induced microstructure evolution from micro/nano-pillar experiments.

Given that none of the available imaging techniques can capture the in-depth microstructure evolution during indentation, modeling stands as the only viable tool to address this need. Current modeling efforts mainly rely on either atomistic simulations using molecular dynamics (MD) or the finite-element-based crystal plasticity approach. At the nano-scale, MD is particularly effective for investigating the processes of twin nucleation, growth, propagation and its interaction with various slip modes, e.g., [19,22,23]. On the other hand, at a sufficiently high scale, where spatial heterogeneities within the twin microstructure can be reasonably disregarded, deformation twinning is typically modeled via the crystal plasticity approach, such that twins are treated as additional (pseudo-)slip systems, and thereby, the twin microstructure is represented in an average sense. Indeed, the crystal plasticity approach has been widely utilized to corroborate various aspects of inelastic deformation during indentation experiments, including the propensity towards twin formation at different indentation depths and declination angles [6,11,12,24], the distribution of twins and dislocation slips beneath the indenter [17], and the characterization of the twin nucleation and slip activation stresses [25]. While these studies provide important quantitative support for experimental observations, they fall short in explicitly representing the twin-boundary interfaces, leaving the true intricacies of the evolving twin microstructure unaccounted for.

Recently, the phase-field method has made its way into the modeling of deformation twinning. It offers a robust computational scheme based on the notion of diffuse interfaces, where continuous (non-conserved) order parameters are employed to distinguish between the twinned and untwinned regions, with their evolution governed by the Ginzburg–Landau-type equation [26]. The diffuse interfaces carry the interfacial energy associated with twin boundaries, and as a result, introduce an internal length-scale into the problem. This renders the phase-field method particularly useful for examining the size effects associated with deformation twinning. The method is ideally suited at an intermediate scale between the nano and macro levels, where resolving the spatial structure of twin boundaries is relevant. Moreover, it overcomes the space and time limitations of atomistic simulations and allows for the simulation of twin microstructure at practical scales.

The integration of the phase-field method with crystal plasticity has opened up new avenues for exploring the coupled evolution of twinning and plastic slip. To date, a number of models have been built within this framework, e.g., [27–30], including our recently-developed model based on

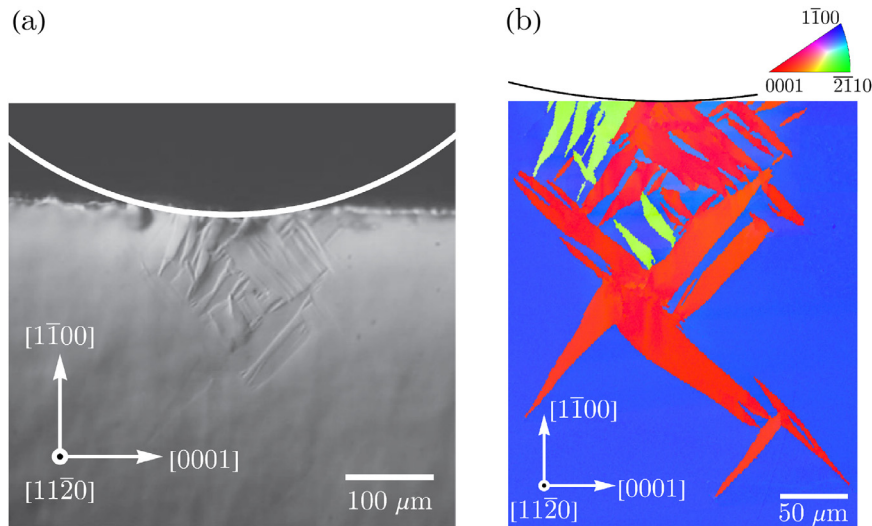


Fig. 1. Indentation-induced twin microstructure in pure magnesium obtained in the experiment of Kitahara et al. [17]: (a) cross-sectional optical micrograph, and (b) the corresponding EBSD inverse pole figure (IPF) map (reproduced with permission from Elsevier). The colors in the IPF show the vertical orientation of the sample with respect to the crystal lattice, as indicated by the stereographic triangle. The EBSD map in panel (b) reveals the presence of two families of twins, distinguished by different colors.

finite-deformation theory [31]. A distinct feature of our model lies in the treatment of the kinematics of deformation twinning, which, rather than being expressed as a conventional shear-based deformation, is formulated as a sequential operation of an isochoric stretch and a rigid-body rotation. This reformulation has also been adopted by others, in the context of coupled twinning and plastic slip [32], as well as in the context of twinning only [33]. The constitutive description of our model follows a variational form, defined in terms of the Helmholtz free energy function and the dissipation potential. The capability of the model to capture the nucleation, growth and propagation of twins, their interaction with plastic slip, and the twin's transmission across the grain boundaries has been demonstrated in the previous work [31]. A subsequent investigation [34] expanded on the computational aspects. Therein, the incremental energy formulation and computational treatments were elaborated and a detailed numerical study was carried out to assess the efficiency and performance of different finite-element discretizations.

Building upon this foundation, we here employ the model to simulate the evolution of indentation-induced twin microstructure in magnesium. To the best of our knowledge, this study marks the first continuum-based modeling effort to spatially-resolved twin microstructures during the indentation while accounting for plastic slip. Our computational study focuses on two specific aspects: (i) indentation at various declination angles, with the aim to investigate the orientation-dependent indentation behavior, and (ii) indentation size effects. Both aspects are systematically addressed, yielding results that align, to some extent, with prior experimental observations, while also providing fresh insights into the indentation-induced deformation behavior of the material. To further explore the size effects, the original model is promoted by switching from conventional crystal plasticity to

gradient-enhanced crystal plasticity. As far as we are aware, this is the first time that the gradient-enhanced crystal plasticity joins forces with the phase-field method for microstructure evolution. Upon an efficient finite-element implementation of the extended model, a robust modeling framework is established that allows for a more holistic analysis of the indentation size effects, with the interfacial energy of twin boundaries and the gradient plasticity acting as the (coupled) sources of size effects.

The remainder of the paper is organized as follows. Details of the model formulation and finite-element treatment are provided in Section 2. The results of our computational study are reported in Section 3. Finally, concluding remarks are given in Section 4.

## 2. Phase-field model of twinning coupled with crystal plasticity

A brief overview of the original model and its extension to gradient crystal plasticity are provided in Sections 2.1 and 2.2, respectively. The micromorphic regularization, which is a pivotal element of the computational model, is discussed in Section 2.3. Finally, the finite-element implementation is outlined in Section 2.4.

### 2.1. The original model

We limit our discussion to a concise presentation of the original model, with its main ingredients summarized in Table 1. To begin with, let us briefly recapitulate the stretch-based kinematics of deformation twinning. In line with the objectives of the current investigation, we focus our attention on one tensile twin variant, encompassing two conjugate twinning systems ( $i = 1, 2$ ), in magnesium with an HCP crystal

Table 1  
Phase-field model of twinning coupled with crystal plasticity: a summary of the original model formulation.

Model unknowns	
$\boldsymbol{\varphi}$	deformation mapping from reference to current configuration
$\eta$	order parameter (twin volume fraction), $0 \leq \eta \leq 1$
$\dot{\gamma}_m^s, \dot{\gamma}_p^s$	slip rate of the slip system $s$ in the matrix (m) and twin (p)
Model equations	
<i>Kinematics</i>	
(T.1)	$\mathbf{F} = \mathbf{F}_e \mathbf{F}_{in}$ multiplicative decomposition of the deformation gradient $\mathbf{F} = \nabla \boldsymbol{\varphi}$
(T.2)	$\mathbf{L}_{in} = \dot{\mathbf{F}}_{in} \mathbf{F}_{in}^{-1} = \mathbf{L}_m + \mathbf{L}_p + \mathbf{L}_{tw}$ inelastic velocity gradient $\mathbf{L}_{in}$
(T.3)	$\mathbf{L}_m = (1 - \eta) \sum_{s=1}^{n_s} \dot{\gamma}_m^s \mathbf{s}_m^s \otimes \mathbf{n}_m^s$ – contribution from plastic slip in the matrix
(T.4)	$\mathbf{L}_p = \eta \sum_{s=1}^{n_s} \dot{\gamma}_p^s \mathbf{s}_p^s \otimes \mathbf{n}_p^s$ – contribution from plastic slip in the twin
(T.5)	$\mathbf{L}_{tw} = \dot{\eta} \log \mathbf{U}_{tw}$ – contribution from deformation twinning
<i>Free energy</i>	
(T.6)	$\psi = \psi_{el} + \psi_h + \psi_\Gamma$ free energy function
(T.7)	$\psi_{el} = \frac{1}{2} \mathbf{H}_e \cdot \mathbb{L} \mathbf{H}_e, \mathbf{H}_e = \frac{1}{2} \log(\mathbf{F}_e^T \mathbf{F}_e)$ – Hencky-type elastic strain energy
(T.8)	$\mathbb{L} = (1 - \eta) \mathbb{L}_m + \eta \mathbb{L}_p$ – fourth-rank elasticity tensor
(T.9)	$\psi_h = \frac{1}{2} H \bar{\gamma}^2$ – stored energy leading to isotropic (linear) hardening
(T.10)	$\dot{\bar{\gamma}} = (1 - \eta) \sum_{s=1}^{n_s}  \dot{\gamma}_m^s  + \eta \sum_{s=1}^{n_s}  \dot{\gamma}_p^s $ – accumulated plastic slip
(T.11)	$\psi_\Gamma = \frac{4\Gamma}{\pi \ell} (\eta(1 - \eta) + \ell^2 \nabla \eta \cdot \nabla \eta)$ – interfacial energy (double-obstacle potential)
<i>Dissipation</i>	
(T.12)	$D = D_m + D_p + D_{tw}$ dissipation potential
(T.13)	$D_m = (1 - \eta) \sum_{s=1}^{n_s} \tau_m^{c,s} \left(  \dot{\gamma}_m^s  + \frac{(\dot{\gamma}_m^s)^2}{2\dot{\gamma}_0} \right)$ – contribution from plastic slip in the matrix
(T.14)	$D_p = \eta \sum_{s=1}^{n_s} \tau_p^{c,s} \left(  \dot{\gamma}_p^s  + \frac{(\dot{\gamma}_p^s)^2}{2\dot{\gamma}_0} \right)$ – contribution from plastic slip in the twin
(T.15)	$D_{tw} = \tau_{tw}^c \gamma_{tw} \left(  \dot{\eta}  + \frac{\dot{\eta}^2}{2\dot{\eta}_0} \right)$ – contribution from deformation twinning
Model constants	
$\mathbf{s}_m^s, \mathbf{s}_p^s$	slip direction of the slip system $s$ in the matrix and twin
$\mathbf{n}_m^s, \mathbf{n}_p^s$	slip plane-normal of the system $s$ in the matrix and twin
$\mathbf{U}_{tw}$	deformation twinning stretch tensor
$\mathbb{L}_m, \mathbb{L}_p$	fourth-rank elasticity tensor of the pure matrix and twin
$H$	isotropic hardening coefficient
$\Gamma$	twin-boundary interfacial energy density
$\ell$	twin-boundary interface thickness parameter
$\tau_m^{c,s}, \tau_p^{c,s}$	CRSS of the slip system $s$ in the matrix and twin
$\tau_{tw}^c$	CRSS for deformation twinning
$\dot{\gamma}_0$	reference slip rate
$\dot{\eta}_0$	reference twinning rate

structure. In the conventional approach, the inelastic deformation associated with each twinning system  $i$  is described by a simple shear,

$$\mathbf{F}_{tw}^{(i)} = \mathbf{I} + \gamma_{tw} \mathbf{a}^{(i)} \otimes \mathbf{m}^{(i)},$$

$$\gamma_{tw} = \frac{\alpha^2 - 1}{\alpha} = \frac{\sqrt{3}a}{c} - \frac{c}{\sqrt{3}a}, \quad \alpha = \frac{\sqrt{3}a}{c} > 1, \quad (1)$$

where  $\mathbf{a}^{(i)}$  and  $\mathbf{m}^{(i)}$  are, respectively, the twinning shear direction and twin plane normal,  $\gamma_{tw}$  is the shear magnitude, and  $a$  and  $c$  are lattice constants. The two conjugate twinning

systems share the same plane of shear, i.e., the vectors  $\mathbf{a}^{(1)}$ ,  $\mathbf{m}^{(1)}$ ,  $\mathbf{a}^{(2)}$ , and  $\mathbf{m}^{(2)}$  are coplanar.

Using the polar decomposition,  $\mathbf{F}_{tw}^{(i)}$  can be uniquely resolved into a volume-preserving stretch  $\mathbf{U}_{tw}^{(i)}$  and a rigid-body rotation  $\mathbf{R}_{tw}^{(i)}$ ,

$$\mathbf{F}_{tw}^{(i)} = \mathbf{R}_{tw}^{(i)} \mathbf{U}_{tw}^{(i)}. \quad (2)$$

It can be readily shown that

$$\mathbf{U}_{tw}^{(1)} = \mathbf{U}_{tw}^{(2)} = \mathbf{U}_{tw}, \quad \mathbf{R}_{tw}^{(1)} = (\mathbf{R}_{tw}^{(2)})^T = \mathbf{R}_{tw}, \quad (3)$$

thus

$$\mathbf{F}_{\text{tw}}^{(1)} = \mathbf{R}_{\text{tw}} \mathbf{U}_{\text{tw}}, \quad \mathbf{F}_{\text{tw}}^{(2)} = \mathbf{R}_{\text{tw}}^T \mathbf{U}_{\text{tw}}. \quad (4)$$

This signifies that the conventional shear-based kinematics, involving two distinct shear deformations for the two conjugate twinning systems, can be reformulated into the stretch-based kinematics, where the two conjugate twinning systems feature an identical stretch  $\mathbf{U}_{\text{tw}}$  while being distinguished by their rigid-body rotations  $\mathbf{R}_{\text{tw}}$  and  $\mathbf{R}_{\text{tw}}^T$ .

Note that within the sharp-interface description, the stretch-based and shear-based approaches are fully equivalent. This equivalence, however, does not extend to the diffuse-interface (phase-field) description due to the incompatibilities present within the diffuse interfaces, see Remark 2.5 in [31] for a more detailed discussion, see also [32,33]. In the phase-field framework, the stretch-based kinematics offers a distinct computational advantage over its shear-based counterpart, as it allows the two conjugate twinning systems to be described in an equivalent manner using just a single order parameter [31]. While this advantage may appear less significant in a 2D setting, it becomes significant in the full 3D setting, where the model must account for three pairs of conjugate twinning systems in HCP crystals and for six pairs in FCC and BCC crystals.

Let us now introduce the phase-field order parameter  $\eta$ , which describes the twin volume fraction, with  $\eta = 0$  representing the matrix (untwinned material),  $\eta = 1$  representing the twin, and  $0 < \eta < 1$  representing diffuse matrix–twin interfaces. In the context of coupled twinning and plasticity, the inelastic deformation gradient  $\mathbf{F}_{\text{in}}$  arises from the plastic slip in the matrix, deformation twinning, and plastic slip in the twin. The contributions of plastic slip to the inelastic velocity gradient  $\mathbf{L}_{\text{in}}$ , namely  $\mathbf{L}_{\text{m}}$  (for plastic slip in the matrix) and  $\mathbf{L}_{\text{p}}$  (for plastic slip in the twin), are derived from the classical crystal plasticity theory and include the weights  $(1 - \eta)$  and  $\eta$ , respectively, see Eqs. (T.3) and (T.4) in Table 1. To illustrate the contribution of deformation twinning,  $\mathbf{L}_{\text{tw}}$ , let us consider the scenario of twinning only, i.e., without plastic slip, where  $\mathbf{F}_{\text{in}} = \mathbf{F}_{\text{tw}}(\eta)$  such that  $\mathbf{F}_{\text{tw}}$  depends now on  $\eta$  within diffuse interfaces. Consistent with the stretch-based kinematics,  $\mathbf{F}_{\text{tw}}$  is defined such that  $\mathbf{F}_{\text{tw}} = \mathbf{I}$  when  $\eta = 0$  and  $\mathbf{F}_{\text{tw}} = \mathbf{U}_{\text{tw}}$  when  $\eta = 1$ , and it is appropriately interpolated between these values when  $0 < \eta < 1$ . Among the possible choices, the logarithmic mixing is selected for  $\mathbf{F}_{\text{tw}}$  [35],

$$\mathbf{F}_{\text{tw}}(\eta) = \exp(\eta \log \mathbf{U}_{\text{tw}}), \quad (5)$$

which leads to

$$\mathbf{L}_{\text{tw}} = \dot{\mathbf{F}}_{\text{tw}} \mathbf{F}_{\text{tw}}^{-1} = \dot{\eta} \log \mathbf{U}_{\text{tw}}. \quad (6)$$

Eq. (6) is then used as the contribution of deformation twinning to the inelastic velocity gradient  $\mathbf{L}_{\text{in}}$  in the general case of twinning and plastic slip, Eq. (T.2). It is important to note that the rigid-body rotations  $\mathbf{R}_{\text{tw}}^{(i)}$  do not enter the kinematics of inelastic deformation. Instead, they contribute to the elastic deformation gradient  $\mathbf{F}_{\text{e}}$ , emerging as a part of the solution to preserve the displacement continuity.

The model possesses a variational structure, with the Helmholtz free energy  $\psi$  and the dissipation potential  $D$  as

the main constituents. The free energy function  $\psi$  comprises the elastic strain energy  $\psi_{\text{el}}$ , stored energy induced by plastic slip (stored energy of cold work)  $\psi_{\text{h}}$ , and twin-boundary interfacial energy  $\psi_{\Gamma}$ . A Hencky-type elastic strain energy  $\psi_{\text{el}}$  is adopted, Eq. (T.7),  $\psi_{\text{h}}$  is defined as a quadratic function of the accumulated plastic slip  $\bar{\gamma}$ , Eqs. (T.9) and (T.10), leading to an isotropic (linear) hardening law, and  $\psi_{\Gamma}$  takes the form of the double-obstacle potential, Eq. (T.11), with parameters  $\Gamma$  and  $\ell$  characterizing the energy and thickness of the diffuse interfaces, respectively. At the same time, the dissipation potential  $D$  accounts for the contributions from plastic slip in the matrix, deformation twinning, and plastic slip in the twin, with each contribution defined as a mixture of viscous and rate-independent dissipation terms, Eqs. (T.12)–(T.15). The global counterparts of the Helmholtz free energy function,  $\Psi = \int_B \psi \, dV$ , and of the dissipation potential,  $\mathcal{D} = \int_B D \, dV$ , are subsequently derived and used to construct the global rate potential  $\Pi$ . The solution of the problem is then obtained by minimizing  $\Pi$  with respect to the problem unknowns, namely the rates  $\dot{\phi}$ ,  $\dot{\boldsymbol{\gamma}}$  and  $\dot{\eta}$ , viz.,

$$\Pi = \dot{\Psi} + \mathcal{D} + \dot{\Omega} \rightarrow \min_{\dot{\phi}, \dot{\boldsymbol{\gamma}}, \dot{\eta}} \quad (7)$$

where  $\dot{\boldsymbol{\gamma}} = \{\dot{\boldsymbol{\gamma}}_{\text{m}}, \dot{\boldsymbol{\gamma}}_{\text{p}}\}$  collects the slip rates associated with the matrix and with the twin,  $\dot{\boldsymbol{\gamma}}_{\text{m}} = \{\dot{\gamma}_{\text{m}}^1, \dots, \dot{\gamma}_{\text{m}}^{n_{\text{s}}}\}$  and  $\dot{\boldsymbol{\gamma}}_{\text{p}} = \{\dot{\gamma}_{\text{p}}^1, \dots, \dot{\gamma}_{\text{p}}^{n_{\text{s}}}\}$ , and  $\Omega$  denotes the potential of the external loads (assumed conservative).

The minimization problem (7) yields the governing equations of the rate problem. Specifically, minimizing  $\Pi$  with respect to  $\dot{\phi}$  establishes the weak form of mechanical equilibrium (virtual work principle), and minimization with respect to the slip rates  $\dot{\boldsymbol{\gamma}}$  and with respect to the rate of the order parameter  $\dot{\eta}$  gives rise to Perzyna-type evolution equations for the corresponding rates, each characterized by a rate-independent threshold and a viscous contribution proportional to the overstress. The explicit forms of the governing equations are not provided here, see [31] for details.

**Remark 2.1.** The evolution law for the order parameter  $\eta$  allows for both its increase and decrease, corresponding to twinning and detwinning, respectively, with both processes being treated identically in the model. Detwinning may proceed either by reverse motion of an existing twin boundary or by nucleation of the matrix phase (a kind of a secondary twin) within an existing twin. In the present context of indentation, the former mechanism is observed, albeit weakly, while the latter is not observed.

**Remark 2.2.** The present model eliminates the need for a particular treatment of twin nucleation. This is because the order parameter ( $\eta$ ) itself is used as the interpolation function within the logarithmic mixing rule (5), rather than a special nonlinear polynomial of  $\eta$  as commonly employed in phase-field models of twinning [28,30,36,37]. Consequently, twin nucleation occurs automatically once the twin transformation condition is met, i.e., once the total driving force for twinning at  $\eta = 0$  (or at  $\eta = 1$  for detwinning) surpasses the rate-independent threshold  $\tau_{\text{tw}}^{\text{c}} \gamma_{\text{tw}}$ , cf. Eq. (T.15). In the indentation

problem studied here, an inhomogeneous stress state naturally develops beneath the indenter, and this is sufficient to trigger twin nucleation. Note, however, that the nucleation stress depends on the interface thickness parameter  $\ell$  and cannot be controlled independently. A more physically plausible strategy would be to decouple the twin nucleation and twin evolution processes, for instance, by introducing an independent twin nucleation model [37]. For a more detailed discussion on this aspect of the model, the reader is referred to Remark 3.1 and Section 5.3 in our previous study [31].

## 2.2. Extension to gradient-enhanced crystal plasticity

The original model discussed above is based on the conventional (size-invariant) crystal plasticity theory. Accordingly, the potential size effects are solely attributed to twinning, arising from the size-dependent contribution of the interfacial energy of twin boundaries. To account for the size effects related to plastic slip, the model is here extended to gradient-enhanced crystal plasticity. This enhancement follows the simplified approach of Wulfinghoff and Böhlke [38], see also [39], where only the gradient of the accumulated plastic slip,  $\nabla\bar{\gamma}$ , enters the constitutive equations. Although more sophisticated approaches based on various measures of plastic strain incompatibility or gradients of individual dislocation densities are more appropriate from a physical standpoint, see e.g., [40–45] as representative examples, they are more complex and increase considerably the cost of the finite-element computations, and are thus not pursued here.

To incorporate the gradient effects, an additional energy term  $\psi_g$  is defined as a quadratic function of  $\nabla\bar{\gamma}$ , taking the form

$$\psi_g = \frac{1}{2} A \nabla\bar{\gamma} \cdot \nabla\bar{\gamma}, \quad (8)$$

where  $A > 0$  represents the corresponding gradient energy coefficient. The new term  $\psi_g$  is then added to the total free energy function  $\psi$ , thus  $\psi = \psi_{el} + \psi_h + \psi_\Gamma + \psi_g$ , cf. Eq. (T.6). This, as a result, introduces a characteristic length  $\ell_g$  into the model, defined as  $\ell_g = \sqrt{A/H}$ , where  $H$  is the isotropic hardening modulus, see Eq. (T.9). In fact, the parameter  $\ell_g$  determines the spatial scale at which the material exhibits size-dependent plasticity.

## 2.3. Micromorphic regularization

The finite-element implementation of the present model is particularly challenging due to the inherent complexities involved. The complexities arise from the strong coupling in the evolution equations of twinning and plastic slips, the presence of the non-differentiable rate-independent dissipation contributions, the bound constraints on the order parameter  $\eta$ , and last but not least, the extension to gradient crystal plasticity. Direct implementation of the model specified above is not straightforward, if possible at all, and an efficient strategy is to resort to the micromorphic regularization technique, as introduced by Forest [46], which significantly facilitates the

finite-element treatment. In our previous study involving the original model with conventional crystal plasticity [31], the micromorphic regularization was applied to the phase-field order parameter  $\eta$  only. Here, with the extension to gradient crystal plasticity, we apply the regularization to both the order parameter  $\eta$  and the accumulated plastic slip  $\bar{\gamma}$ . For earlier applications of the micromorphic regularization to gradient crystal plasticity, see [38,39,47].

The micromorphic regularization is performed by introducing additional degrees of freedom, specifically  $\eta_\chi$  and  $\bar{\gamma}_\chi$ , which are conjugate to the order parameter  $\eta$  and to the accumulated plastic slip  $\bar{\gamma}$ , respectively. The equality between the original variables and their micromorphic counterparts is enforced via the penalty method. To this end, a penalty term,  $\psi_{pen}$ , is defined and is added to the free energy  $\psi$ ,

$$\psi_{pen} = \frac{1}{2} \chi_\eta (\eta - \eta_\chi)^2 + \frac{1}{2} \chi_\gamma (\bar{\gamma} - \bar{\gamma}_\chi)^2, \quad (9)$$

where  $\chi_\eta$  and  $\chi_\gamma$  are the penalty parameters. This enforcement can be also done by using Lagrange multipliers [38,39], however, the penalty method is here preferred due to its simplicity and satisfactory performance. Next, the gradient of the order parameter,  $\nabla\eta$ , in the interfacial energy term  $\psi_\Gamma$ , and the gradient of the accumulated plastic slip,  $\nabla\bar{\gamma}$ , in the gradient energy term  $\psi_g$  are replaced by the gradients of their micromorphic counterparts. The corresponding energy terms are thus redefined as

$$\psi_\Gamma = \frac{4\Gamma}{\pi\ell} (\eta(1-\eta) + \ell^2 \nabla\eta_\chi \cdot \nabla\eta_\chi), \quad (10)$$

and

$$\psi_g = \frac{1}{2} A \nabla\bar{\gamma}_\chi \cdot \nabla\bar{\gamma}_\chi. \quad (11)$$

With their gradients removed from the constitutive equations, the variables  $\eta$  and  $\bar{\gamma}$  can be considered as local variables and their evolution equations can be solved at the local integration-point level, enabling a more efficient handling of the associated complexities. It is worth noting that in the finite-element computations, the penalty parameters  $\chi_\eta$  and  $\chi_\gamma$  are chosen sufficiently large to ensure a close correlation between the original variables and the micromorphic counterparts, and thereby, to effectively capture the related gradient effects.

## 2.4. Finite-element implementation

We now briefly discuss the main aspects of the finite-element implementation. For a more detailed discussion, readers are referred to [34]. The implementation begins by the time-discretization of the rate problem. The time-integration scheme is based on the implicit backward-Euler method. The rate variables, the accumulated plastic slip  $\bar{\gamma}$ , and the dissipation potential  $D$  are approximated by the respective incremental forms. To compute the (current) inelastic deformation gradient  $\mathbf{F}_{in}$ , see Eq. (T.2), a volume-preserving exponential mapping is adopted [48,49]. The problem at hand possesses a local–global structure. At the local level, the unknowns are

the order parameter and slip increments, namely  $\Delta\eta$ ,  $\Delta\gamma_m^s$  and  $\Delta\gamma_p^s$ , while the global unknowns consist of the displacement  $\mathbf{u} = \boldsymbol{\varphi} - \mathbf{X}$  and the micromorphic variables  $\eta_x$  and  $\bar{\gamma}_x$ . This structure prompts an iterative–subiterative solution strategy, wherein both the global and local problems are solved by means of the Newton method.

A crucial aspect that demands careful consideration is the non-differentiability of the local problem, which stems from the rate-independent dissipation contributions, Eqs. (T.13)–(T.15), the inequality constraints on the order parameter  $\eta$ ,  $0 \leq \eta \leq 1$ , and the absolute-value function in the equation for the accumulated plastic slip, cf. Eq. (T.10). The augmented Lagrangian method is employed to overcome the non-differentiability associated with the rate-independent dissipation and with the inequality constraints [50]. Moreover, we expand the model to consider  $2n_s$  slip systems (separately within the matrix and twin) by accounting for positive and negative slip directions, thus restricting the slip increments to be non-negative. This, as a result, eliminates the need for the absolute-value function in the calculation of the accumulated plastic slip  $\bar{\gamma}$ . It is important to note that this representation, although more costly as it doubles the number of plastic slip unknowns, was found crucial for the successful implementation of the gradient crystal plasticity. Without it, the model would suffer from severe convergence issues.

The finite-element simulations in the present study pertain to a 2D plane-strain indentation problem. Thus, for spatial discretization, 8-noded elements with quadratic serendipity shape functions (and a reduced  $2 \times 2$  Gauss integration rule) are used for the displacement, while 4-noded elements with linear shape functions are used for the micromorphic variables. This specific element combination is selected due to its superior efficiency [34]. Meanwhile, the contact problem of indentation is solved by satisfying the unilateral contact condition at the potential contact surface. The indenter is assumed as a rigid and frictionless cylinder. Hence, only the normal contact condition is enforced, and this is done by the augmented Lagrangian method [51].

The model is written as a computer code within the *Mathematica* package *AceGen* and the finite-element simulations are carried out in *AceFEM* [52]. Upon leveraging the automatic differentiation and code simplification attributes of *AceGen*, the computer coding process is greatly streamlined and the efficiency of the resulting computational model is significantly enhanced. It is worth noting that our simulations address a wide range of problem sizes, as detailed in Section 3.4, with the most computationally demanding cases involving over 10 million degrees of freedom. Without an efficient implementation, successful completion of such large simulations would not be feasible.

### 3. Indentation of a magnesium single-crystal

In this section, we present and discuss the simulation results for the indentation of a magnesium single-crystal. The setup of the problem, including the geometry, mesh, material parameters and loading, is described in Section 3.1. We be-

gin the analysis by showcasing the results of a representative simulation in Section 3.2, which serves as a basis for subsequent analyses and comparisons. Section 3.3 investigates the indentation behavior across various crystal orientations. Indentation size-effects are the subject of the study in Section 3.4. The results presented in these sections are obtained using the model with conventional crystal plasticity, i.e., with no gradient plasticity effects. Finally, in Section 3.5, we incorporate the gradient-enhanced crystal plasticity and revisit the size effects.

#### 3.1. Setup of the problem

A schematic of the problem under study is presented in Fig. 2(a). The problem concerns the indentation of a magnesium single-crystal within a rectangular domain of dimensions  $2L \times L = 40 \times 20 \mu\text{m}^2$ . A rigid cylindrical indenter, with a radius  $R = 2 \mu\text{m}$ , is pressed against the top edge of the domain at its center. Note that the indenter radius and domain size specified above pertain to the studies reported in Sections 3.2 and 3.3. In the study of size effects in Sections 3.4 and 3.5, the dimensions are scaled proportionally, as specified in Section 3.4.

The simulations account for one loading–unloading cycle, with the indentation speed set to  $V_{\text{ind}} = 50 \text{ nm/s}$ . In all the simulations, the loading continues until the normalized indentation depth reaches  $\delta/R = 0.06$ . Boundary conditions are applied such that all edges, except the top edge undergoing indentation, are constrained to zero displacement in the respective normal direction. A non-uniform finite-element mesh is employed, with the highest mesh density in the region beneath the indenter where the microstructure develops (the central rectangular region with the dimensions of  $3.3 \times 5 \mu\text{m}^2$ ) and with a gradual coarsening of the mesh away from this region, see Fig. 2(a). Note that a very coarse mesh is shown in Fig. 2(a), and a much finer mesh is used in the computations, as specified below. The domain is chosen large enough to eliminate the artificial effects of the boundaries on the results, while the computational cost is significantly reduced via the mesh coarsening. The element size  $h$  in the finest mesh region is defined in relation to the twin-boundary interface thickness parameter  $\ell$ . To properly capture the intricate microstructural features, a ratio of  $\ell/h = 1.3$  is fixed, leading to a ratio of about  $\pi\ell/h = 4$ , with  $\pi\ell$  denoting the theoretical (stress-free) interface thickness.

The operative conjugate twinning systems and the operative slip systems are illustrated in Fig. 2(b). Following our previous study [31], a single twin deformation variant, corresponding to two conjugate twinning systems, is considered in our 2D plane-strain problem. Specifically, we focus on the pair with the twin plane normals  $(10\bar{1}2)$  and  $(\bar{1}012)$ . This configuration places our 2D plane strain problem within the  $(\bar{1}2\bar{1}0)$  plane, which corresponds to the plane of shear of the selected conjugate twinning systems. The sketch in Fig. 2(b) shows the two twin planes and the plane of shear, the latter depicted in gray. Three effective slip systems are considered, namely one (easy) basal slip system and two symmetric (hard)

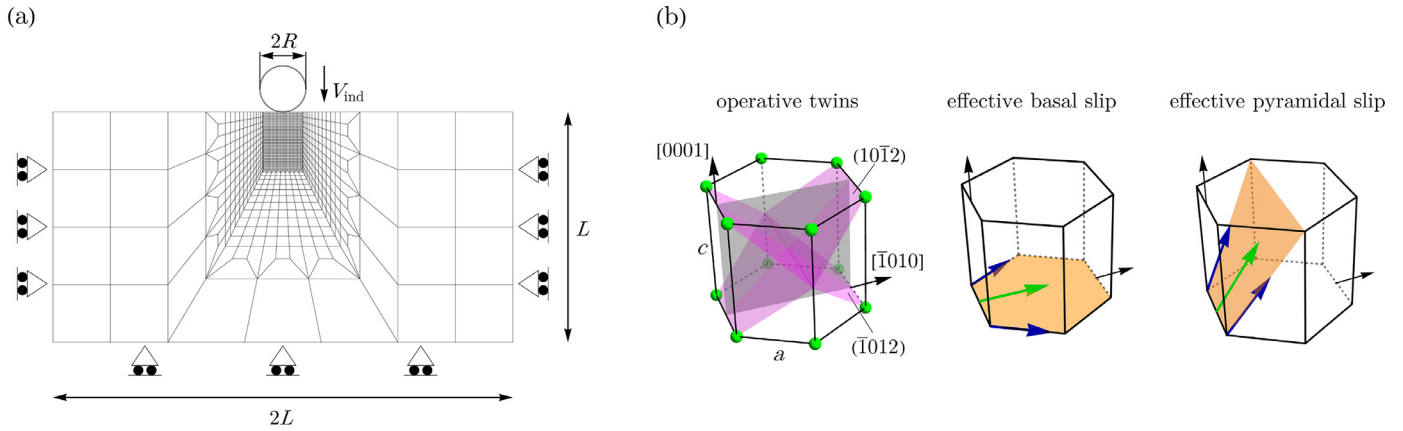


Fig. 2. (a) Setup of the 2D indentation problem, and (b) operative twins and slip systems in our 2D plane strain configuration. For a better illustration, panel (a) displays a much coarser mesh than the one used in the actual computations. In panel (b), only one effective pyramidal slip system is shown, as the second one resides symmetrically with respect to it. Note also that the gray plane depicted in panel (b) indicates the plane of our 2D simulations.

pyramidal slip systems. Each effective basal/pyramidal slip system represents two co-planar (concurrently-active) crystallographic basal/pyramidal slip systems, as illustrated in Fig. 2(b). The effective  $(0001)[\bar{1}010]$  basal slip system considered is representative of two co-planar basal slip systems with  $[\bar{2}110]$  and  $[\bar{1}\bar{1}20]$  slip directions. Similarly, the effective  $(10\bar{1}1)[\bar{1}012]$  and  $(\bar{1}011)[10\bar{1}2]$  pyramidal slip systems account for two  $\langle a+c \rangle$  pyramidal slip systems each, the former for the co-planar  $(10\bar{1}1)[\bar{2}\bar{1}13]$  and  $(10\bar{1}1)[\bar{1}\bar{1}23]$  slip systems and the latter for the co-planar  $(\bar{1}011)[2\bar{1}\bar{1}3]$  and  $(\bar{1}011)[11\bar{2}3]$  slip systems. Note that other slip systems, for instance, the prismatic slip systems, cannot be considered in the 2D plane strain setup adopted here, as they would necessarily induce an out-of-plane strain component, thus violating the plane-strain conditions.

The material parameters used in the simulations are typical for magnesium. The twinning shear magnitude  $\gamma_{tw} = 0.129$  is derived from the lattice parameters ratio of  $c/a = 1.624$ . The critical resolved shear stress (CRSS) for twinning is adopted as  $\tau_{tw}^c = 15$  MPa. Identical CRSS values are assumed for plastic slips in the matrix and in the twin. Specifically, for the effective basal slip we use  $\tau_m^{c,b} = \tau_p^{c,b} = 15$  MPa, i.e., equal to that of twinning, and for the effective pyramidal slips we use  $\tau_m^{c,p} = \tau_p^{c,p} = 150$  MPa. The magnesium HCP crystal structure is regarded as having a transversely isotropic elasticity, with five independent elastic constants taken as  $c_{11} = 63.5$  GPa,  $c_{33} = 66.5$  GPa,  $c_{12} = 25.9$  GPa,  $c_{13} = 21.7$  GPa and  $c_{44} = 18.4$  GPa. The isotropic hardening coefficient is set to  $H = 0.4$  GPa. The twin-boundary interfacial energy is adopted as  $\Gamma = 0.15$  J/m<sup>2</sup>, and the interface thickness parameter as  $\ell = 10$  nm (note that in the study of size effects in Sections 3.4 and 3.5, the parameter  $\ell$  takes also other values). The reference slip rate is chosen as  $\dot{\gamma}_0 = 1$  s<sup>-1</sup>, while the reference twinning rate of about  $\dot{\eta}_0 = 20$  s<sup>-1</sup> is calculated from the reference interface propagation speed,  $v_0 = 500$  nm/s, according to the relation  $\dot{\eta}_0 = \pi v_0 / 8\ell$  [31], see also [53]. Moreover, the micromorphic penalty parameter is taken as  $\chi_\eta = 2$  GPa. All these parameters are the same as those in our pre-

vious study [31], where detailed justifications and references are provided. The exceptions are the interface thickness parameter  $\ell$  and the micromorphic penalty parameter  $\chi_\eta$ .

Parameter  $\ell$  has been carefully adjusted to ensure that the twin microstructure is not overly diffuse, and at the same time, the computational effort is manageable. Recall that the ratio between the element size  $h$  and  $\ell$  is fixed at  $\ell/h = 1.3$  within the finest-mesh region, leading to an element size of  $h = 7.7$  nm, and thus  $432 \times 576$  elements in this region.

Concerning the micromorphic penalty parameter  $\chi_\eta$ , a detailed parametric study reported in [34] demonstrates that the simulation results remain practically insensitive to the value of  $\chi_\eta$  for  $\chi_\eta > 0.5$  GPa. However, when  $\chi_\eta$  is increased well beyond this limit, a substantial rise in the computational cost is observed, see Section 4.3 in [34]. Based on these indications, a value of  $\chi_\eta = 2$  GPa is adopted in this work, which is somewhat lower than the value of 5 GPa used in our previous modeling study [31]. The computational cost is thus reduced compared to that study, while the accuracy of the results is not compromised.

Finally, the parameter governing the gradient plasticity effects is set to  $A = 0.4$  GPa  $\mu\text{m}^2$ , so that the corresponding length scale is obtained as  $\ell_g = 1$   $\mu\text{m}$ . In addition, the related micromorphic penalty parameter is calibrated as  $\chi_\gamma = 100$  GPa.

It is of note that our initial analyses confirm that, with the rate parameters  $\dot{\gamma}_0 = 1$  s<sup>-1</sup> and  $\dot{\eta}_0 = 20$  s<sup>-1</sup> and the indentation speed  $V_{ind} = 50$  nm/s assigned here, the viscous effects are not noticeable. This conclusion has been drawn by increasing/decreasing the indentation speed  $V_{ind}$  by a factor of 10, and observing no major changes in the simulation results, particularly in terms of the microstructure evolution. However, increasing the speed by a factor of 100 does introduce noticeable rate effects. The simulations are thus carried out close to the rate-independent limit. It is important to stress that too low rate effects can adversely influence the performance of the Newton method. Therefore, the parameters controlling the rate effects must be carefully calibrated to achieve an optimal

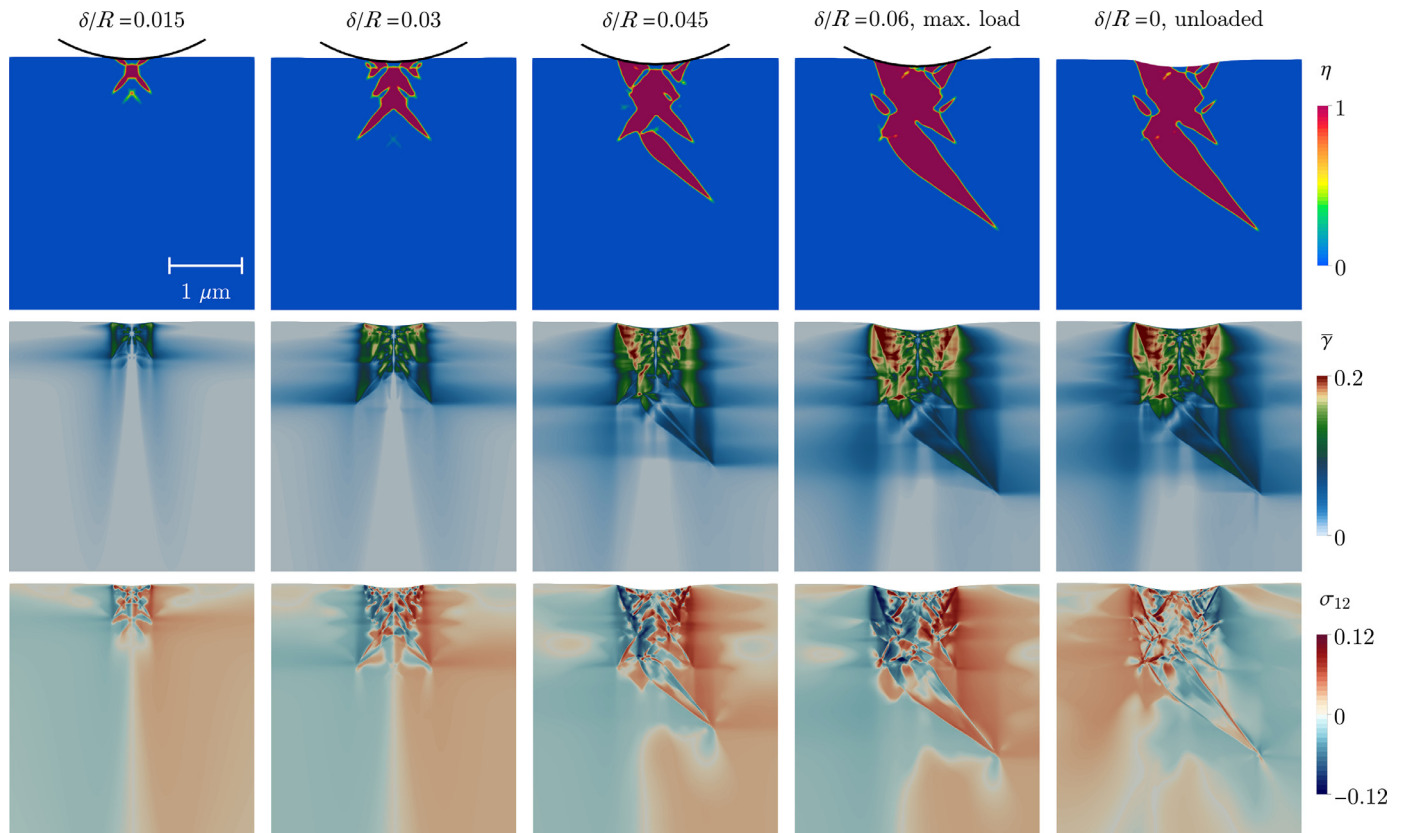


Fig. 3. Indentation of a magnesium single-crystal with a declination angle of  $\theta_0 = 90^\circ$ : evolution snapshots of twin microstructure (top), accumulated plastic slip (middle) and shear stress (bottom). Here and in the subsequent figures, the stress is given in GPa.

balance between accuracy and computational efficiency, see the related discussion in [34].

### 3.2. Microstructure evolution and mechanical response

We begin by analyzing the indentation-induced microstructure for the crystal lattice oriented at  $\theta_0 = 90^\circ$ , where  $\theta_0$  refers to the angle between the crystal's  $c$ -axis and the indentation loading direction and is typically referred to as declination angle. This orientation is the most favorable for the activation of tensile twins. Fig. 3 illustrates the evolution of the twin microstructure, plastic slip activity, and shear stress for selected indentation depths  $\delta$ . The twin microstructure is represented by the spatial distribution of the twin volume fraction  $\eta$ , plastic slip activity is simply represented by the accumulated plastic slip  $\bar{\gamma}$ , and the shear stress by the respective component of the Cauchy stress tensor,  $\sigma_{12}$  (in GPa). Here and in the remaining figures, the spatial distributions are displayed only in the vicinity of the indenter.

Of particular interest in Fig. 3 is the evolution of twin microstructure. The initial microstructure appears by the formation of a scissors-shaped twin beneath the indenter. The microstructure evolves, in an apparently symmetric manner, until around halfway through the indentation loading, i.e., up to the normalized indentation depth of about  $\delta/R = 0.03$ . During this stage, the evolution is marked by the nucleation of a

new scissors-shaped twin beneath the existing twin domain. However, upon further loading, the microstructure breaks the symmetry (a more detailed analysis of the symmetry breakdown is provided in Appendix A). From this point forward, the evolution shifts towards the growth of a single lenticular-shaped twin, rather than the nucleation of new twins. It is noteworthy that the individual arms of the scissors-shaped twins form an angle of about  $42^\circ$  with respect to the indentation direction, which is close to the theoretical matrix-twin interface orientation of  $43.2^\circ$ .

The evolution of the twin microstructure and its spatial inhomogeneity have a significant impact on the accumulated slip ( $\bar{\gamma}$ ) and stress ( $\sigma_{12}$ ) distributions beneath the indenter. As shown in Fig. 3, both fields develop highly inhomogeneous patterns which are synchronized with the evolving twin microstructure. However, both  $\bar{\gamma}$  and  $\sigma_{12}$  exhibit additional fine-scale features that extend beyond the resolution of the twin microstructure. These fine features seem to be related to the local stress redistribution associated with abrupt events such as twin nucleation and interface annihilation. Plastic slip thus proceeds in a highly inhomogeneous manner, and the related incompatibility of the plastic strain induces fine-scale inhomogeneity of the stress, which persists upon unloading, resulting in a highly non-uniform residual stress distribution. Note that such level of detail is available thanks to the spatially-resolved modeling of twinning, as delivered by the phase-field

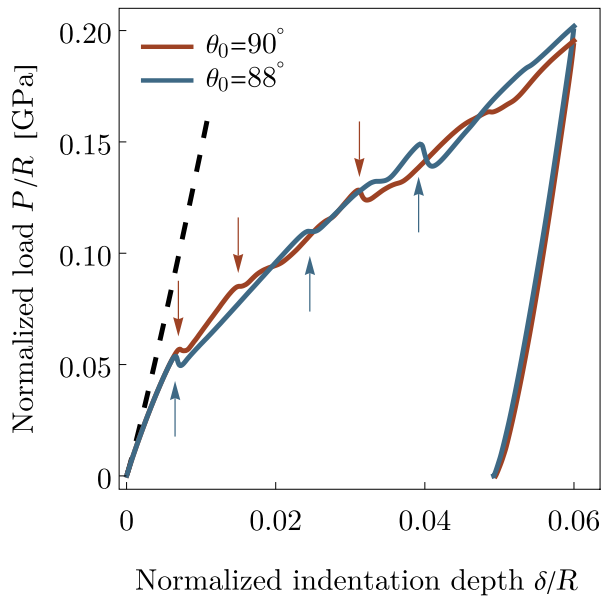


Fig. 4. Normalized indentation load–depth ( $P/R$ – $\delta/R$ ) response for two slightly different declination angles. The black dashed line represents the elastic response (almost identical for the two declination angles). The vertical arrows indicate the sudden load changes associated with major twin nucleation events.

method, and is not achievable in the mean-field-like crystal plasticity approaches that treat twinning as a pseudo-slip [54]. Recall that Fig. 3 shows only the region in the vicinity of the indenter, and both  $\bar{\gamma}$  and  $\sigma_{12}$  gradually fade to zero as they approach the boundary of the actual computational domain.

During unloading, the deformation remains predominantly elastic, characterized by a significant stress relaxation and no discernible change in the twin microstructure and plastic slip activity. In fact, unloading is accompanied by weak detwinning, which occurs through a slight reverse motion of twin boundaries. The related changes in the microstructure are hardly visible in Fig. 3, and a detailed comparison would be needed to reveal the changes in the interface positions. Overall, it has been checked that the total volume of twins decreases by 4.3% during unloading (the total volume of twins is calculated by simply integrating the field of  $\eta$ ). A more pronounced detwinning during unloading is observed in some cases studied below, in particular, when gradient plasticity effects are included in the model. The maximum load and the stresses are then noticeably higher, and stress relaxation during unloading induces more pronounced detwinning. Anyway, the related changes in the appearance of the microstructure are still not significant, and this effect is thus not examined in detail.

The indentation load–depth response shown in Fig. 4 reveals interesting observations that aid in characterizing the indentation-induced inelastic deformation. The foremost observation from Fig. 4 is that each twin nucleation is associated with a sudden load drop in the response (see the arrows). These load drops resemble pop-ins which are commonly ob-

served in the experiments and are linked to the twin nucleation events, e.g., [6,8,9]. In fact, in our simulation, each instance of twin nucleation or rearrangement during the loading process is registered as a distinct load event in Fig. 4. Since the indentation process is here controlled by prescribing the position of the indenter (kinematic control), the nucleation events are accompanied by load drops. In the case of force-control indentation, commonly applied in experiments, such abrupt microstructural events induce pop-ins, i.e., sudden increase of the indentation depth at an approximately constant load, see the related discussion in [55]. It is important to note that pop-ins can be also linked to the activation of dislocations, e.g., [10,56]. However, within the continuum crystal plasticity framework adopted here, dislocation pop-ins cannot be described. As can be seen in Fig. 4, plastic slip precedes the first twin nucleation, with its onset characterized by a gradual deviation from the purely elastic response, see the dashed line.

Despite the symmetry of the system implied by the declination angle of  $\theta_0 = 90^\circ$ , the twin microstructure evolution in Fig. 3 exhibits the breakdown of symmetry, as a way to reduce the incremental work supplied to the system, see Appendix A. The precise control of the declination angle is, however, difficult in practice, and a certain degree of misalignment is typically unavoidable [14,57]. This would thus essentially lead to the development of non-symmetric microstructures right from the start. To explore the effect of a slight misalignment of the crystal, an additional simulation is carried out for  $\theta_0 = 88^\circ$ , i.e., deviating by  $2^\circ$  from the ideal case. The corresponding indentation load–depth response is compared with that of  $\theta_0 = 90^\circ$  in Fig. 4, while the evolution of the resulting twin microstructure, plastic slip and shear stress is illustrated in Fig. 5. It follows that, although the twin morphology obtained for  $\theta_0 = 88^\circ$  is obviously different than that of  $\theta_0 = 90^\circ$ , the plastic slip activity and the intensity of shear stress remain quite similar (see Fig. 3). However, the fine-scale inhomogeneity of both the accumulated slip  $\bar{\gamma}$  and the shear stress  $\sigma_{12}$  is less pronounced compared to the symmetric case of  $\theta_0 = 90^\circ$ . It can be seen that the twin microstructure evolves in a non-symmetric manner from the very onset, through the nucleation of a lenticular-shaped domain, see the left-most snapshots in Fig. 5 (our auxiliary simulation for a declination angle of  $\theta_0 = 89.75^\circ$  confirms that even a minor deviation of  $0.25^\circ$  from  $90^\circ$  is sufficient to trigger a non-symmetric twin microstructure initiation and evolution). The entire twin evolution process is then characterized by three major nucleations, with twins nucleating consistently as lenticular-shaped domains. Each newly-nucleated twin is oriented almost perpendicular to the preceding one, thus creating a zigzag pattern of nucleation. At the same time, the indentation load–depth responses (see Fig. 4) follow a consistent overall trend. Of course, given the different twin microstructures, the distinct load events occur at different indentation depths, causing some variations between the two curves. During unloading, the two curves almost coincide and end up at nearly the same residual indentation depth,  $\delta/R \approx 0.05$ .

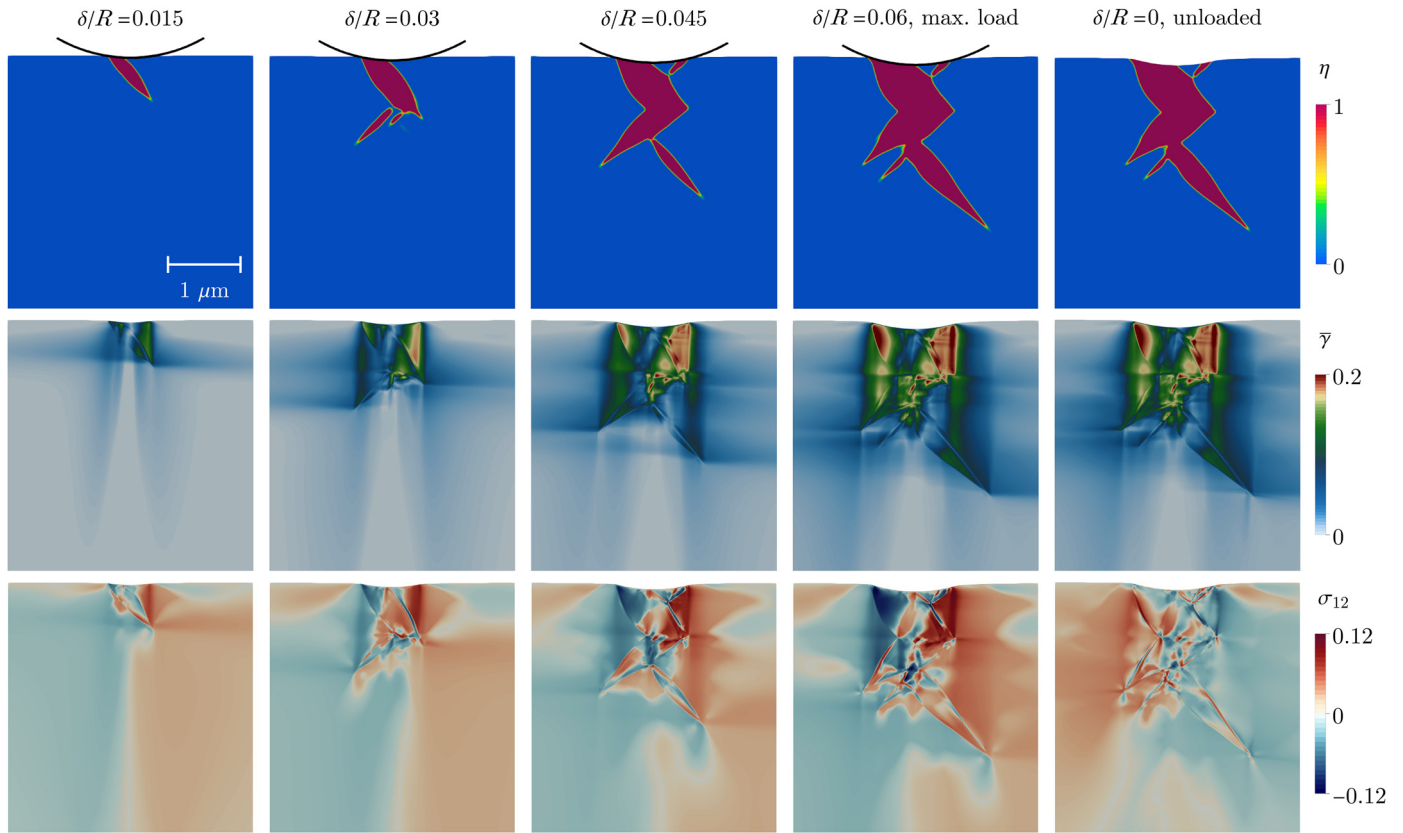


Fig. 5. Indentation of a magnesium single-crystal with a declination angle of  $\theta_0 = 88^\circ$ : evolution snapshots of twin microstructure (top), accumulated plastic slip (middle) and shear stress (bottom).

### 3.3. Indentation at different declination angles

Several experimental studies on magnesium have found that the indentation-induced microstructure and mechanical response are greatly influenced by the declination angle, e.g., [10,12,14,17,58,59]. This effect arises from the highly anisotropic behavior of the material, whereby indenting along different crystallographic orientations alters the propensity of the material to deform by twinning or plastic slip.

The aim of the analysis in this section is thus to delineate the role of declination angle  $\theta_0$  in controlling the deformation mechanism. We examine the declination angle  $\theta_0$  within the range from  $\theta_0 = 0^\circ$  (with the  $c$ -axis parallel to the indentation direction) to  $\theta_0 \approx 90^\circ$  (with the  $c$ -axis nearly perpendicular to the indentation direction). A summary of the simulation results is presented in Fig. 6. Here, the twin microstructure is represented by the spatial distribution of the lattice orientation angle  $\theta_{\text{lat}}$ , defined as the angle between the indentation direction and the  $c$ -axis in the deformed configuration. This representation enables us to visualize the lattice reorientation effects caused by twinning and plastic slip within the microstructure.

It is important to recognize that for  $\theta_0 = 0^\circ$  the predominantly compressive deformation induced by the indentation load cannot be accommodated by (tensile) twinning nor by basal slip with vanishing Schmid factors. Accordingly, only

the (hard) pyramidal slip can accommodate such deformation, possibly with small contribution of the basal slip compensating local incompatibilities. Accordingly, the indentation load is the highest for  $\theta_0 = 0^\circ$ , Fig. 6(a). At the same time, it is evident in Fig. 6(b) that no twinning is activated for  $\theta_0 = 0^\circ$  and only plastic slip is evolved. The crystallographic symmetry characteristic for the declination angle  $\theta_0 = 0^\circ$  implies that plastic slip evolves in a symmetric manner, while the shear stress  $\sigma_{12}$  is anti-symmetric, with equal magnitudes on the left and right sides of the indent but opposite signs. Since there is no twinning, both fields do not exhibit the fine-scale inhomogeneities discussed earlier in the case of  $\theta_0 = 90^\circ$  and also observed for other declination angles, see Fig. 6(b).

As mentioned above, for  $\theta_0 = 0^\circ$ , compression along the  $c$ -axis does not favor twinning in the area beneath the indenter. In fact, experiments [9,13] and theoretical analysis [13] indicate that tensile twins can appear at the sides of the indent, although typically at higher indentation depths. While no twinning is observed for  $\theta_0 = 0^\circ$  in the present simulations, an additional simulation carried out for  $\ell = 40$  nm (not reported here) shows that small diffuse twins are formed at the sides of the indent (note that twin nucleation is easier for larger  $\ell$ ), confirming that a favorable stress state indeed develops in these areas. Accordingly, it is also expected that twinning would be predicted for  $\theta_0 = 0^\circ$  at larger indentation depths and larger indenter radii.

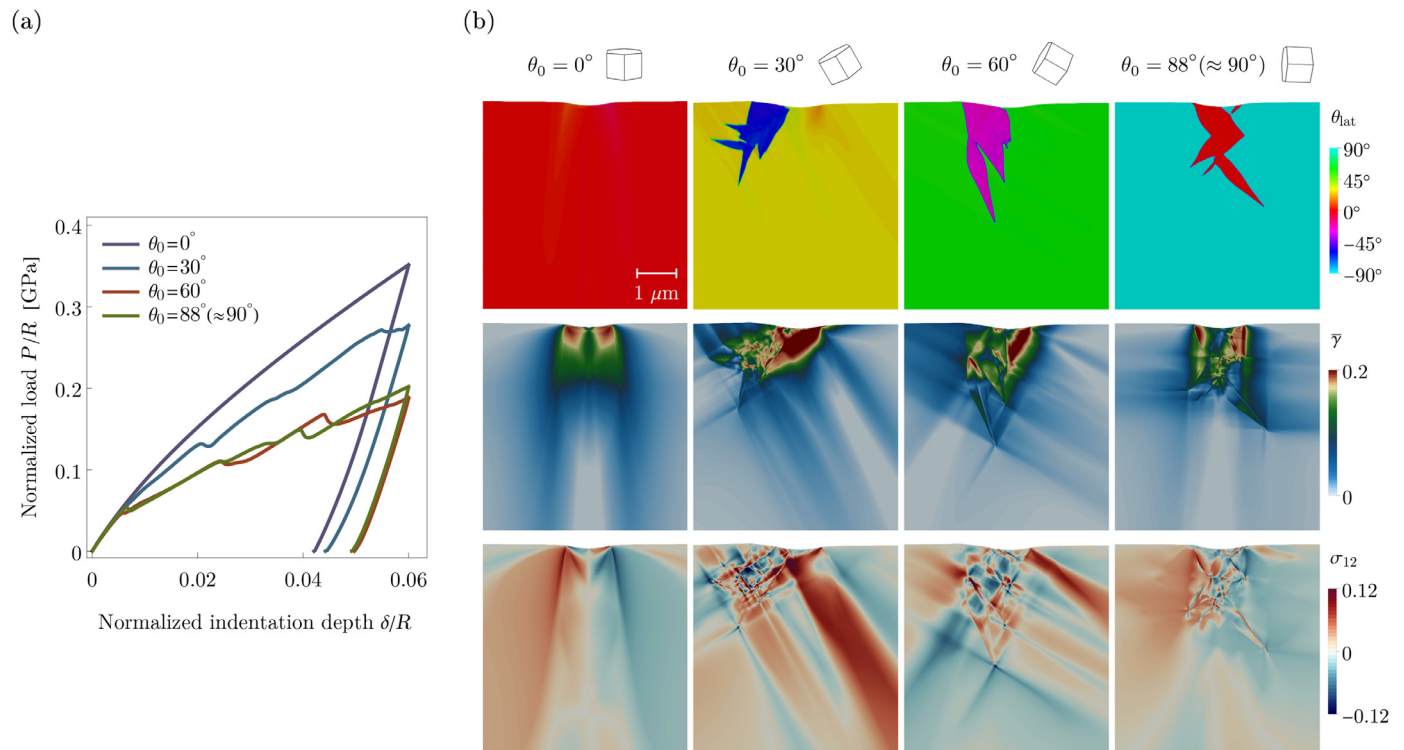


Fig. 6. Effect of declination angle  $\theta_0$  on: (a) the indentation load–depth response, and (b) the microstructural features. In panel (b), the first row depicts the twin microstructure (in terms of the lattice orientation angle  $\theta_{lat}$ ), the second row depicts the plastic slip activity, and the third row depicts the shear stress distribution. The snapshots are taken at the fully-unloaded state.

As  $\theta_0$  increases, twinning becomes more prominent. The evolved twin microstructure then leads to a complex plastic slip pattern and stress distribution, both exhibiting fine-scale inhomogeneities discussed earlier. Interestingly, for  $\theta_0 = 30^\circ$  and  $\theta_0 = 60^\circ$ , twinning is localized at one side of the indent, inducing a distinct pile-up on the surface. This observation agrees with the analysis in [13], see their Fig. 6(b). The opposite side of the indent experiences a profuse activity of plastic slip. Notably, for the case with  $\theta_0 = 30^\circ$ , the side dominated by plastic slip shows traces of lattice rotation (see the related  $\theta_{lat}$  snapshot), which is not observable for  $\theta_0 = 60^\circ$ . The microstructural characteristics observed here and the corresponding effects on the mechanical response resemble, at least to some qualitative extent, the experimental findings [10,12,59].

As commented above,  $\theta_0 = 0^\circ$  demonstrates the largest indentation load, driven by the lack of twinning, a relatively soft inelastic mechanism. Then follows  $\theta_0 = 30^\circ$ , with its maximum indentation load reduced by about 23% compared to  $\theta_0 = 0^\circ$ . Similar hardening rates are captured for  $\theta_0 = 60^\circ$  and  $\theta_0 = 90^\circ$ , with their maximum indentation loads being quite close to each other. To validate the simulation results, we plot in Fig. 7 the variation of the maximum indentation load  $P_{max}$  as a function of the declination angle  $\theta_0$  and compare it with the experimental data of Sánchez-Martín et al. [13]. In line with the experiment, the maximum load for  $\theta_0 = 0^\circ$  (denoted as  $P_0$ ) serves as a normalization factor for  $P_{max}$ . The experimental data correspond to deep indents (with a maximum indentation depth of  $2 \mu\text{m}$ ), and a high degree of twinning activity has been reported. Indeed, a very good agreement between

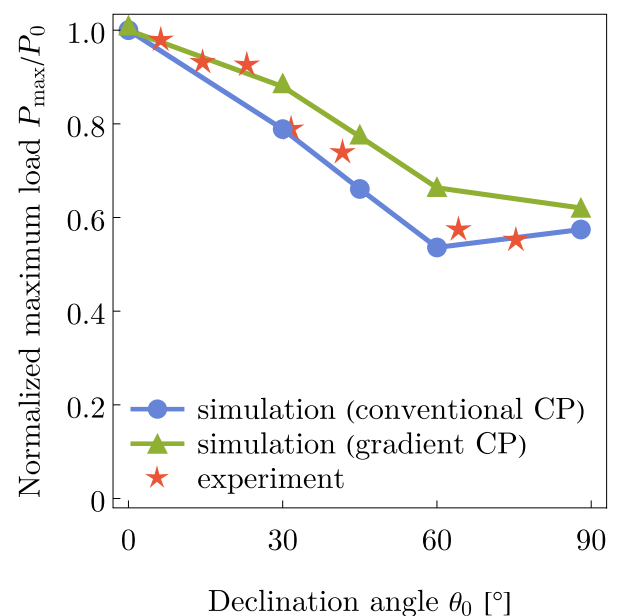


Fig. 7. Variation of maximum indentation load  $P_{max}$  as a function of the declination angle  $\theta_0$ . The load  $P_{max}$  is normalized by the maximum indentation load obtained for the case with  $\theta_0 = 0^\circ$ , which is denoted by  $P_0$ . The experimental data are taken from [13].

the simulation and experimental results is evident. Fig. 7 also presents predictions obtained by the model incorporating gradient plasticity effects (see Section 2.2), which demonstrate a trend consistent with that obtained by the model with con-

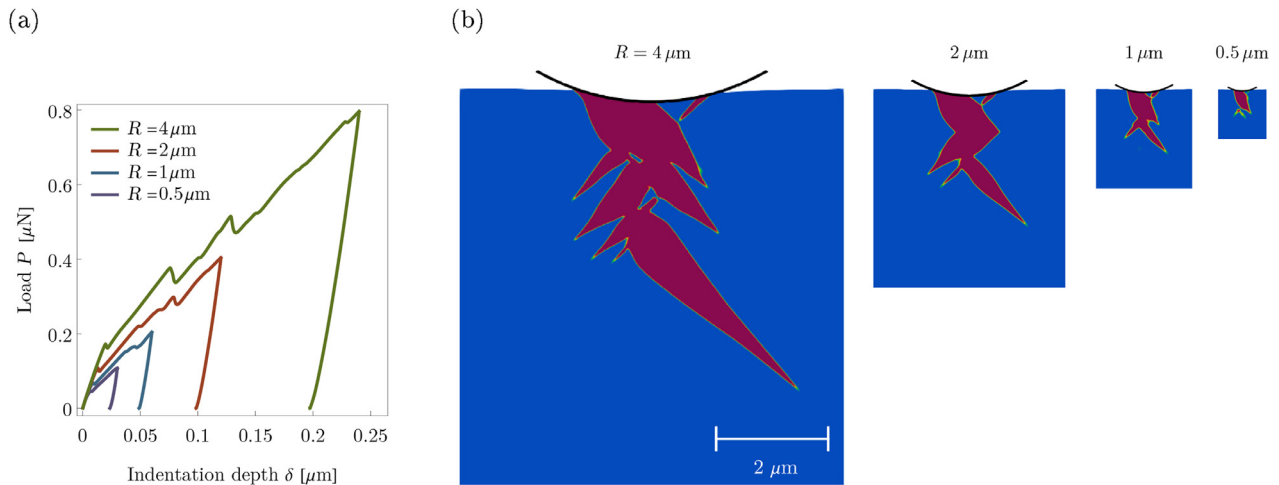


Fig. 8. Indentation size effects with varying indenter radius  $R$ : (a) load–depth ( $P$ – $\delta$ ) responses, and (b) the final twin microstructures. The interface thickness parameter is set to  $\ell = 10$  nm. The scale bar in panel (b) applies to all subfigures.

ventional (non-gradient) plasticity (the corresponding detailed results are reported in [Appendix B](#)). Note that Sánchez-Martín et al. [13] also conducted experiments with shallow indents (maximum indentation depth of  $0.3 \mu\text{m}$ ), where plastic slip dominated and twinning was inhibited. As these experiments did not exhibit significant twinning activity, the corresponding data points have not been included in [Fig. 7](#).

### 3.4. Size effects

It is well-known that under indentation at micron and sub-micron scales, crystalline metals exhibit indentation size effects, manifested by an increase in indentation hardness as the indent size, and accordingly the contact interaction zone, decreases [60] which is often associated with the notion that ‘smaller is stronger’. The size effects are typically attributed to strain gradients and to the related geometrically necessary dislocations (GNDs) [61]. Additionally, twinning, and equally importantly the interplay between twinning and plastic slip, also contribute to size effects, e.g., [15,62,63]. Nevertheless, it appears that the role of twinning in governing the indentation size effects in magnesium has received limited attention, with only a few experimental studies addressing it [11,13,14]. The present analysis is thus devoted to the size effects in relation to indenter radius  $R$ , and correspondingly, in relation to indentation depth  $\delta$ . The analysis is divided in two parts. In the first part, presented in this section, the twin boundary energy acts as the sole source of size effects in the model. The second part, presented in [Section 3.5](#), extends the analysis by incorporating gradient plasticity as an additional source of size effects.

For this analysis, the declination angle of  $\theta_0 = 88^\circ$  is selected. We explore a range of indenter radius, from  $R = 0.5 \mu\text{m}$  to  $R = 16 \mu\text{m}$ . The computational domain  $2L \times L$  is scaled proportionally with  $R$  so that geometrical similarity is preserved, thus  $L = 5 \mu\text{m}$  for  $R = 0.5 \mu\text{m}$  and  $L = 160 \mu\text{m}$  for  $R = 16 \mu\text{m}$ . As explained in [Section 3.1](#), the resolution

of twin-boundary interfaces is maintained by fixing the ratio  $\ell/h = 1.3$  in the finest-mesh region. Given an interface thickness parameter of  $\ell = 10$  nm, the ratio  $\ell/h = 1.3$  would result in too demanding computations for large radii. To mitigate this issue, following previous studies [35,55], we adopt a strategy that involves increasing the interface thickness parameter  $\ell$ , and proportionally, the element size  $h$ . Specifically, three interface thickness parameters are considered, namely  $\ell = 10$  nm,  $\ell = 20$  nm and  $\ell = 40$  nm. This strategy not only allows us to examine large indenter radii but also to assess the impact of  $\ell$  on the simulation results. The reference twinning rate  $\dot{\eta}_0$  is changed in line with  $\ell$  following the relation  $\dot{\eta}_0 = \pi v_0/8\ell$ . At the same time, the indentation speed  $V_{\text{ind}} = 50$  nm/s is maintained across all simulations, and so is the reference slip rate  $\dot{\gamma}_0 = 1 \text{ s}^{-1}$ ; both parameters are the same as in the preceding analyses. Note that the maximum indentation depth is kept fixed at  $\delta_{\text{max}}/R = 0.06$ .

As mentioned above, the element size  $h$  is varied along with  $\ell$ , so that  $h = 7.7$  nm for  $\ell = 10$  nm and  $h = 31$  nm for  $\ell = 40$  nm. On the other hand, for a prescribed element size  $h$ , the total number of elements depends directly on the indenter radius  $R$  (since the dimensions of the problem,  $2L \times L$ , are scaled with  $R$ ). Depending on  $R$  and  $\ell$ , the number of elements within the finest-mesh region thus varies from  $108 \times 144$  to  $864 \times 1152$  and the total number of degrees of freedom varies from 162 thousand to 10.1 million (and from 185 thousand to 11.5 million in the case of the gradient-enhanced crystal plasticity model considered in [Section 3.5](#)).

We begin our discussion with [Fig. 8](#) which illustrates the indentation load–depth response and the final twin microstructure for  $\ell = 10$  nm across various indenter radii  $R$ . Both the microstructure and the indentation response display size effects. Notably, for the smallest indenter radius ( $R = 0.5 \mu\text{m}$ ), the twin microstructure takes on a bulky morphology. The larger the radius  $R$ , the richer the microstructure, such that for the largest radius ( $R = 4 \mu\text{m}$ ), an intriguing branched morphology emerges, with each twin branch having a lenticular

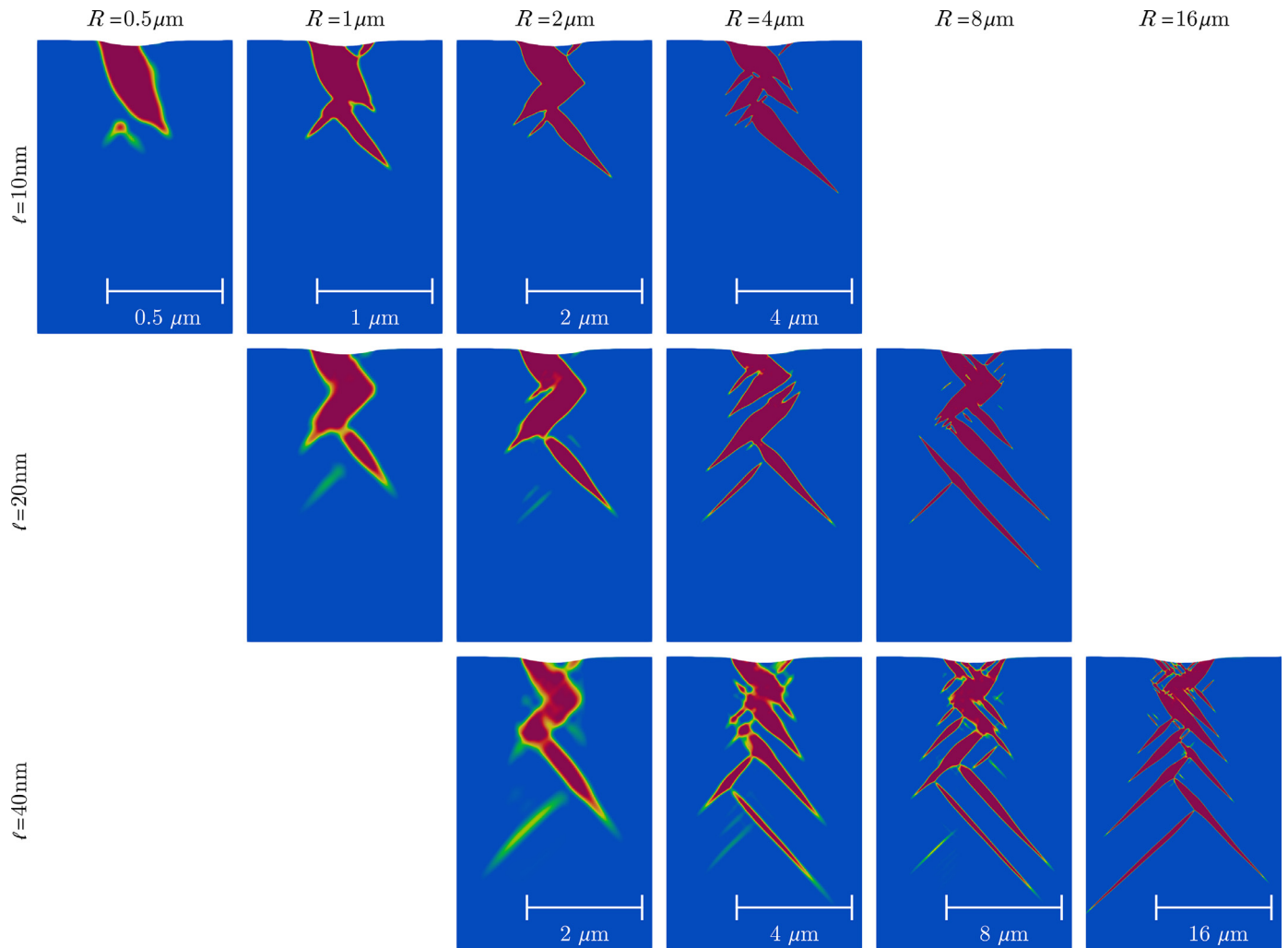


Fig. 9. The final twin microstructure as a function of indenter radius  $R$  and interface thickness parameter  $\ell$ .

shape. In tandem, the indentation load–depth response exhibits more identifiable abrupt load events, each linked to a distinct twin nucleation (or twin rearrangement). This is in contrast to  $R = 0.5 \mu\text{m}$  where the response has a relatively smooth inelastic branch, reflecting the more uniform growth of the twin domain. The rationale behind the observed size effects is traced to the competition between the interfacial energy of twin boundaries and other contributions to the (incremental) energy balance. At smaller spatial scales, the interfacial energy plays a dominant role, prompting the material to minimize its energy by forming fewer twin interfaces. Conversely, at larger spatial scales, the interfacial energy is less dominant and does not prohibit the microstructure from forming twin interfaces.

The same trend of microstructural changes, i.e., from bulky to intricate branched morphology, is observed for other interface thickness parameters,  $\ell = 20 \text{ nm}$  and  $\ell = 40 \text{ nm}$ . Fig. 9 presents the complete map of final twin microstructures for different  $\ell$  and  $R$ . Of particular interest in Fig. 9 are the microstructures that develop a dense network of twin branches, see e.g., the case with  $R = 16 \mu\text{m}$  and  $\ell = 40 \text{ nm}$ .

Interestingly, the twin microstructure extends deep beneath the indent, forming elongated lenticular-shaped domains that are arranged in a zigzag pattern. Such microstructures bear a close qualitative resemblance to the microstructure observed in the experiment of Kitahara et al. [17], see Fig. 1. A supplementary movie showing the complete microstructure evolution for the case with  $R = 16 \mu\text{m}$  and  $\ell = 40 \text{ nm}$  is made available alongside this paper.

Yet another observation from Fig. 9 is the diffuseness of the microstructure as a function of  $\ell$ . While the overall twin morphology remains fairly consistent across different  $\ell$ , the microstructure becomes clearly more diffuse as  $\ell$  increases. Moreover, since  $\ell$  directly influences the energy barrier for twin nucleation (see Remark 2.2 in this paper and Section 5.3 in [31]), larger values of  $\ell$  result in more developed microstructures.

Another important point to mention regards the activity of plastic slip and shear stress distribution in relation to size effects (separate figures illustrating them are not provided). It is essential to acknowledge that the corresponding patterns are closely intertwined with the twin microstructure (see

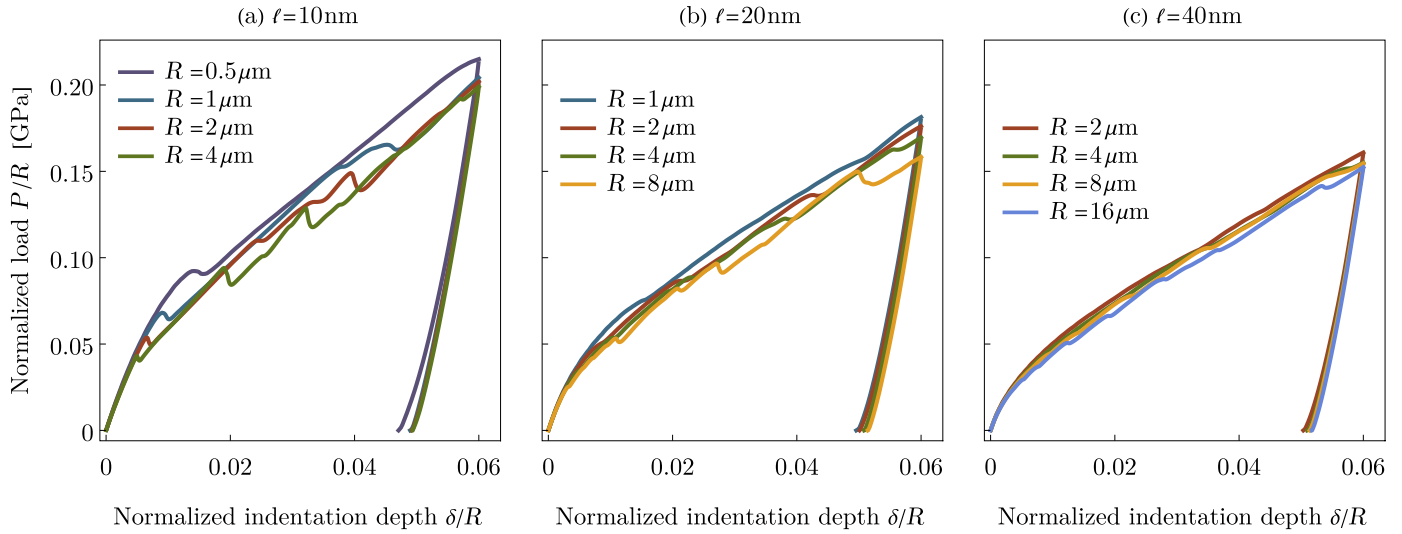


Fig. 10. Normalized indentation load–depth ( $P/R-\delta/R$ ) response as a function of indenter radius  $R$  and interface thickness parameter  $\ell$ .

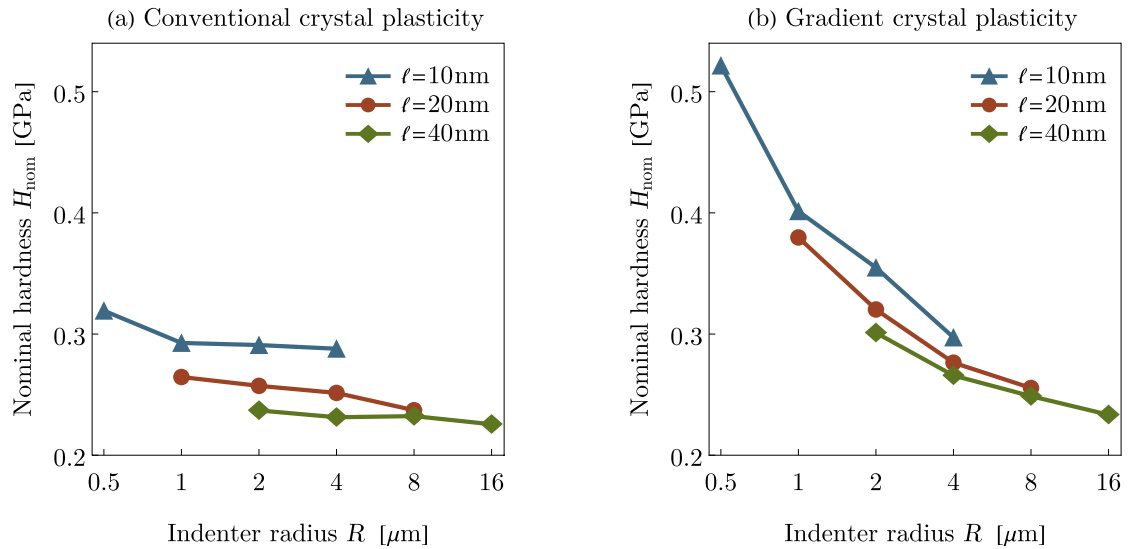


Fig. 11. The effect of the indenter radius  $R$  on the nominal indentation hardness  $H_{\text{nom}}$ : (a) the model with conventional crystal plasticity, and (b) the model with gradient-enhanced crystal plasticity.

the related discussions in Sections 3.2 and 3.3), and thereby, some microstructural adaptations are expected across different  $R$  and  $\ell$ . Yet, the results show that general characteristics, in terms of both distribution and intensity, remain consistent throughout.

The normalized indentation load–depth ( $P/R-\delta/R$ ) responses for various  $\ell$  and  $R$  are compared in Fig. 10. Normalizing by  $R$  filters out the first-order geometrical effects, allowing for a clearer assessment of the size effects in the responses. Somewhat surprisingly, the related effects appear less pronounced than anticipated. However, certain trends remain noticeable, particularly for the smallest  $\ell = 10$  nm. Specifically, it is seen that as  $R$  increases, the normalized load ( $P/R$ ) required for twin nucleation and subsequent growth of twin microstructure decreases. In addition, aside from the smallest radius ( $R = 0.5 \mu\text{m}$ ), the maximum load reached in

all cases is nearly the same, and the difference in the responses is primarily due to the deviation in the location of abrupt load events. A similar observation can be made for other  $\ell$  values, where the responses exhibit even a closer alignment across different radii. To complete our assessment, we provide in Fig. 11(a) the plot of the nominal indentation hardness  $H_{\text{nom}}$  as a function of radius  $R$ . The nominal hardness is defined as  $H_{\text{nom}} = P_{\text{max}}/A_{\text{nom}}$ , with  $A_{\text{nom}} = 2\sqrt{\delta_{\text{max}}(2R - \delta_{\text{max}})} \approx 0.7R$  denoting the nominal contact area associated with the maximum load  $P_{\text{max}}$ . Indeed, Fig. 11(a) confirms the mild size effects reported in Fig. 10.

The size effects discussed above are governed solely by the interfacial energy of twin boundaries, and the general observation is that the microstructure shows a significant size-dependence while the normalized indentation load–depth response and hardness are only weakly affected. A more pro-

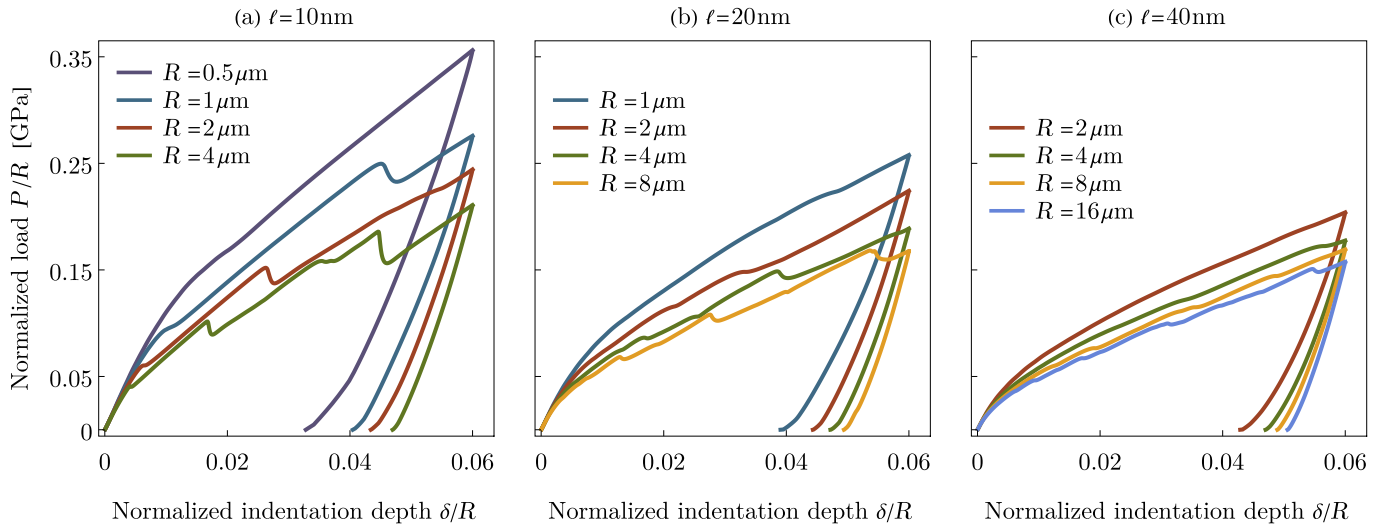


Fig. 12. Indentation size effects captured by the model with gradient-enhanced crystal plasticity: normalized indentation load–depth ( $P/R$ – $\delta/R$ ) response as a function of indenter radius  $R$  and interface thickness parameter  $\ell$ .

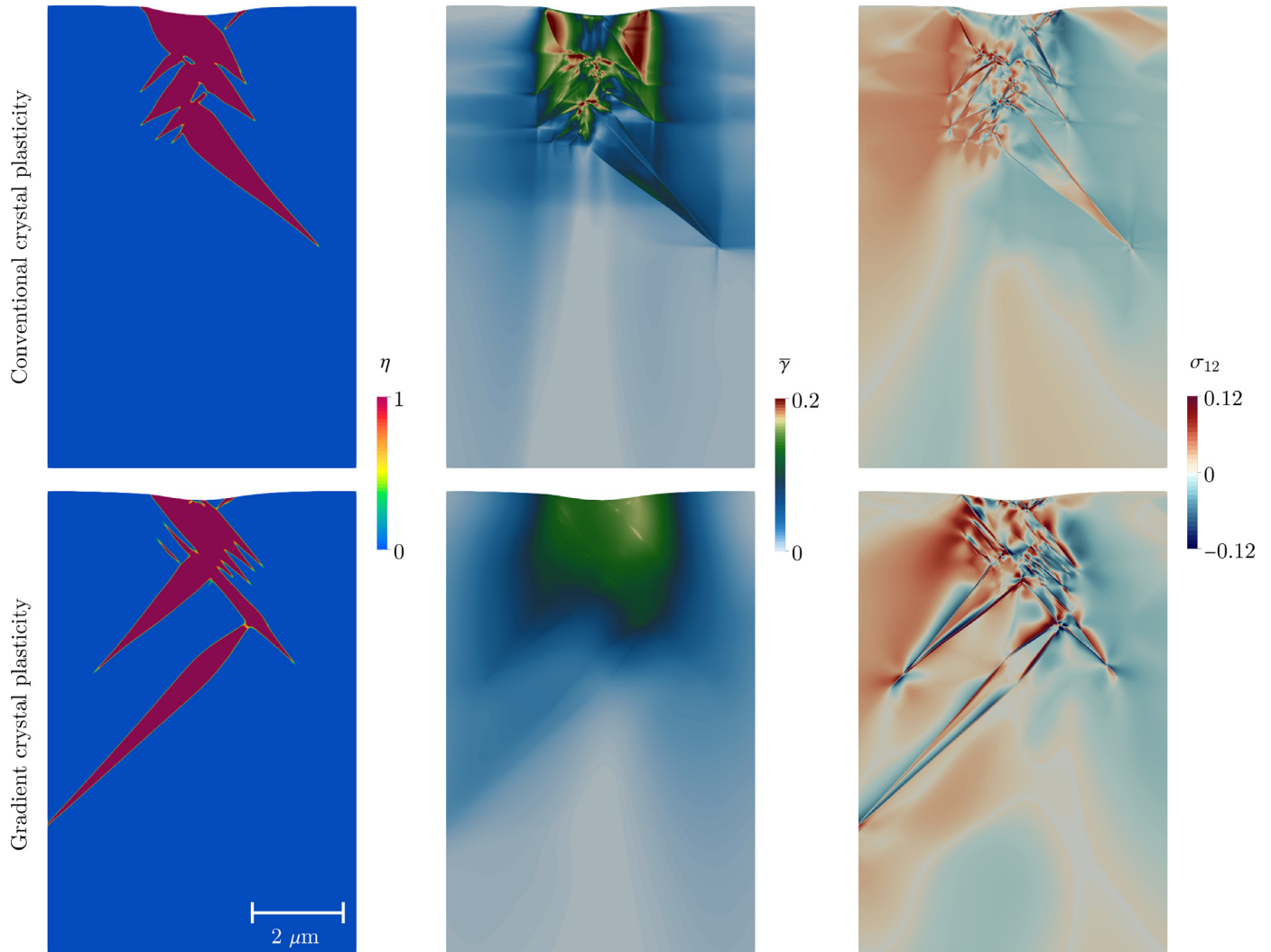


Fig. 13. Comparison of twin microstructure, plastic slip activity and shear stress distribution between the model with conventional crystal plasticity (top row) and the model with gradient-enhanced crystal plasticity (bottom row). The results correspond to simulations with  $R = 4 \mu\text{m}$  and  $\ell = 10$  nm. The snapshots are taken at the fully-unloaded state.

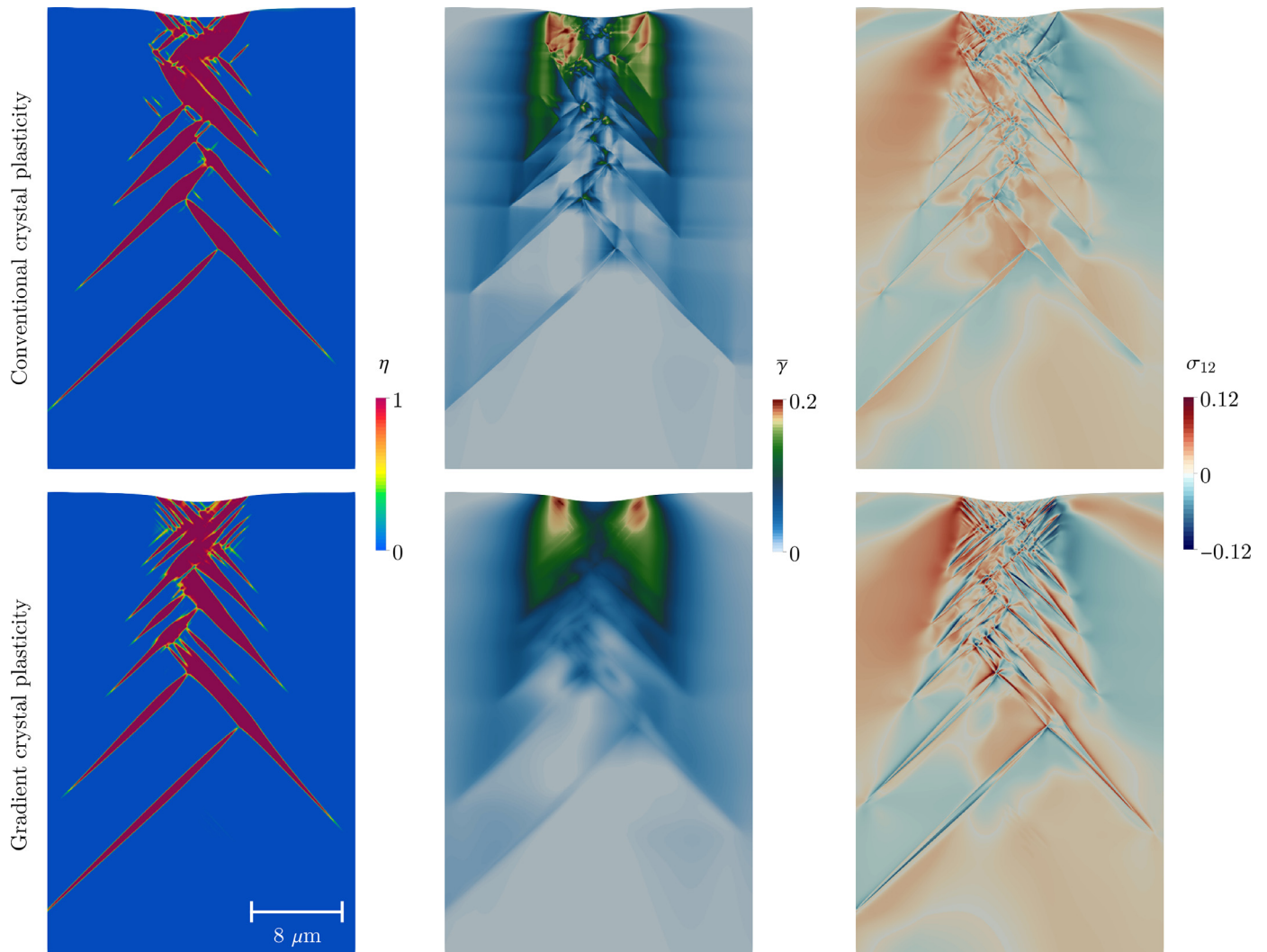


Fig. 14. Comparison of twin microstructure, plastic slip activity and shear stress distribution between the model with conventional crystal plasticity (top row) and the model with gradient-enhanced crystal plasticity (bottom row). The results correspond to simulations with  $R = 16 \mu\text{m}$  and  $\ell = 40 \text{ nm}$ . The snapshots are taken at the fully-unloaded state.

nounced impact of the interfacial energy on the indentation response has been predicted in pseudoelastic shape memory alloys (SMAs) [55]. It is, however, important to note that the martensitic transformation (which is a displacive transformation, just like deformation twinning) stands as the prevailing, if not the only, inelastic mechanism in SMAs, and the contribution of plasticity is then minimal, if not absent. Consequently, the interplay between the size-dependent interfacial energy and the elastic strain energy is more visibly reflected in the resulting indentation load–depth response, and thereby, in the trend of indentation hardness, see [55].

We now direct the attention to Fig. 11(b), where pronounced size effects are evident in the plot of the nominal hardness  $H_{\text{nom}}$  as a function of the indenter radius  $R$ . This emerges as a result of incorporating gradient plasticity as a second key contributor to size effects, see Section 2.2. A detailed discussion of the corresponding results is provided in the following subsection.

### 3.5. Size effects: with the contribution from gradient plasticity

It follows from Fig. 11(b) that incorporating gradient plasticity amplifies the indentation size effect, allowing for a more effective representation of the increase in the indentation hardness with decreasing indenter radius. To gain a deeper insight into the trend illustrated in Fig. 11(b), we examine the corresponding normalized load–depth responses, presented in Fig. 12. A comparison between Fig. 12 and Fig. 10 highlights the substantial impact induced by gradient plasticity on the responses, with the size effects remaining evident even at the largest scale examined.

To conclude our analysis, it is pertinent to examine the microstructure when gradient plasticity effects are at play. For this purpose, we compare the twin microstructure, the activity of plastic slip and the shear stress distribution for the cases with and without gradient plasticity. Comparisons are made

for two indenter radii, namely  $R = 4 \mu\text{m}$  and  $R = 16 \mu\text{m}$ , as shown in Figs. 13 and 14, respectively. The impact of gradient plasticity on the microstructure is obviously more pronounced at the smaller scale of  $R = 4 \mu\text{m}$ . Specifically, the twin microstructure adopts a markedly different morphology, featuring multiple small twin branches and more elongated large twin domains. Moreover, the accumulated plastic slip  $\bar{\gamma}$  displays a more spread-out distribution beneath the indenter, and a reduced magnitude, whereas the shear stress  $\sigma_{12}$  is more intense and exhibits pronounced fine-scale inhomogeneities, as in the case with no gradient plasticity. The observed effects are more weakly produced at the larger scale of  $R = 16 \mu\text{m}$ . Notably, as shown in Fig. 14, while the overall twin morphology remains consistent between the two cases, the incorporation of gradient plasticity results in the formation of small twin branches dispersed across the microstructure, which are otherwise absent.

#### 4. Summary and concluding remarks

The real-time visualization of the indentation-induced microstructure evolution allows to establish the link between microstructural changes and macroscopic events, which is essential for fully characterizing the material's behavior, especially in HCP metals where deformation is highly anisotropic and is dominated by twinning. The phase-field method has emerged as a promising continuum-based computational tool for predicting the twin microstructure. When coupled with crystal plasticity, it offers a viable framework for simulating the complex interplay between deformation twinning and plastic slip. In this study, we leveraged a recently-developed finite-strain model of this kind to simulate the indentation-induced microstructure evolution in a magnesium single-crystal. Finite-element simulations have been carried out in a 2D plane-strain setting, leading to several intriguing findings.

- (i) The foremost attention has been placed on the evolution of twin microstructure during indentation, on the corresponding load–depth response, and on how the plastic slip activity and stress distribution are intricately connected with the twin morphology. It has been observed that each major twin nucleation is marked by a distinct load drop, resembling the pop-in event, in the load–depth response. Interestingly, despite the symmetry of the problem setup imposed by the declination angle of  $\theta_0 = 90^\circ$ , symmetry breaking of the twin microstructure occurs midway through the indentation loading.
- (ii) The simulation results demonstrate an orientation-dependent behavior that aligns with prior experimental observations. As expected, and quite naturally, twinning is most favorable when the indentation is applied perpendicular to the  $c$ -axis, while it is practically suppressed when the indentation is applied parallel to the  $c$ -axis. At intermediate declination angles, twinning is localized on one side of the indent, while the opposite side experiences a profuse activity of plastic slip, a combination of actions that leads to an uneven pile-up

pattern. Moreover, the trend of maximum indentation load as a function of declination angle follows a predictable trajectory, with  $\theta_0 = 0^\circ$  exhibiting the hardest response and  $\theta_0 \approx 90^\circ$  the softest, in a close agreement with the experimental findings of Sánchez-Martín et al. [13].

- (iii) An unexpected yet intriguing outcome emerges from the study of indentation size effects when the interfacial energy of twin boundaries is the sole source of size effects. Although the twin microstructure exhibits clear size-dependent morphology, the corresponding plot of nominal hardness does not adhere to an appreciable ‘smaller is stronger’ trend. Extending the model to incorporate gradient crystal plasticity provides further insight. With the introduction of a length scale of  $\ell_g = 1 \mu\text{m}$ , it becomes clear that gradient plasticity plays a more dominant role in governing size effects, with its impact on the nominal hardness being more pronounced compared to that of the interfacial energy of twin boundaries.
- (iv) A particularly striking outcome of the simulations is the remarkable richness of the twin microstructure at large dimensions. For a sufficiently large indenter radius  $R$  and an appropriately selected interface thickness parameter  $\ell$  (and accordingly, an appropriately selected finite-element mesh density), the resulting microstructure exhibits an intricate array of twin domains, bearing a strong qualitative resemblance to the experimentally-observed remnant twin microstructure of Kitahara et al. [17]. The microstructure is enriched even further when gradient crystal plasticity is incorporated in the model.
- (v) Important to highlight is the dual role of the parameter  $\ell$  in controlling both the diffusivity of the twin interfaces and the driving force for twin nucleation and propagation. Therefore, careful consideration must be given to the choice of  $\ell$ , as an inappropriate selection could compromise the spatial resolution of the microstructure and undermine its physical relevance. A related observation in this respect is that at large spatial scales (when larger  $\ell$  is used), the indentation load–depth response is noticeably smoother compared to small scales. However, when  $\ell$  is chosen such that the interfaces remain reasonably sharp, the major microstructural events, i.e., the nucleation of distinct lenticular-shaped twins, still leave discernible macroscopic signatures, even when they occur deep inside the bulk of the material. This behavior is clearly demonstrated in the supplementary movie. Furthermore, while some experimental studies have noted microstructural changes during indentation unloading [9], our simulations detect such changes only to a negligible extent.

To wrap up the discussion, we stress that our model and simulations pertain to a 2D plane-strain setting, which inherently limits the complexity of the problem. Only one twin variant, representing two conjugate twinning systems, along with three effective slip systems, each representing two concurrently-active slip systems, are considered. Despite these

simplifications, the predictions proved satisfactory, with several aspects aligning with experimental evidence. Nevertheless, more realistic 3D simulations, featuring a more accurate representation of twinning and slip mechanisms, are essential to achieve more insightful and accurate predictions. A full 3D simulation of magnesium with an HCP crystal structure would require the inclusion of three (primary) twin variants and at least 12 slip systems (separately in the matrix and in the twins), which would significantly complicate the model and render the finite-element computations formidably challenging. Efforts towards a 3D extension are currently underway.

### Declaration of competing interest

The authors declare that they have no known competing financial interests or personal relationships that could have appeared to influence the work reported in this article.

### CRediT authorship contribution statement

**Mohsen Rezaee-Hajidehi:** Writing – review & editing, Visualization, Software, Methodology, Investigation, Conceptualization, Writing – original draft. **Przemysław Sadowski:** Writing – review & editing, Visualization, Software, Methodology, Investigation, Conceptualization. **Stanisław Stupkiewicz:** Writing – review & editing, Methodology, Conceptualization.

### Acknowledgment

This work has been partially supported by the National Science Centre (NCN) in Poland through Grant No. 2018/29/B/ST8/00729 and by the EffectFact project (Grant agreement ID: 101008140) funded within the H2020 Programme, MSC Action RISE-2022.

## Appendix A. Twin microstructure: analysis of symmetry breakdown

In this appendix, we carry out a detailed analysis of the microstructure symmetry breakdown observed in Section 3.2 for  $\theta_0 = 90^\circ$ . To this end, an extra simulation has been carried out for one half of the domain with the symmetry conditions enforced along the symmetry axis. This setup effectively enforces development of a symmetric microstructure, thus preventing the symmetry breakdown.

Fig. A.1(a) compares the indentation load–depth curves for the two cases, i.e., the full domain (non-symmetric microstructure) and the half domain (symmetric microstructure). The two curves are apparently identical up to  $\delta/R \approx 0.03$ , marked by letter B. However, a more detailed examination reveals that a bifurcation actually appears earlier, at the instant marked by letter A. This is illustrated in Fig. A.1(b), which shows the difference between the two curves. Indeed, until instant A, the two solutions are identical, see the inset in Fig. A.1(b). Afterwards, the load corresponding to the full domain becomes lower than that corresponding to the half domain. This means that the non-symmetric solution obtained for the full domain is energetically favorable, as the incremental work supplied to the system is lower in the case of non-symmetric microstructure. Note that the load difference is initially small and thus not visible on the overall diagram in Fig. A.1(a), and it becomes visible only after instant B. Actually, the difference changes the sign several times during the evolution, but it is the negative sign of the load difference at the bifurcation point A that confirms that the symmetry breakdown is indeed energetically preferable.

Fig. A.2 shows the microstructures corresponding to instants A, B and C, as well as the final microstructure at the maximum load. The difference between the microstructures at instant B is not directly visible, and only a small difference can be appreciated at instant C, compare the new twins forming below the existing twin structure. The small difference in

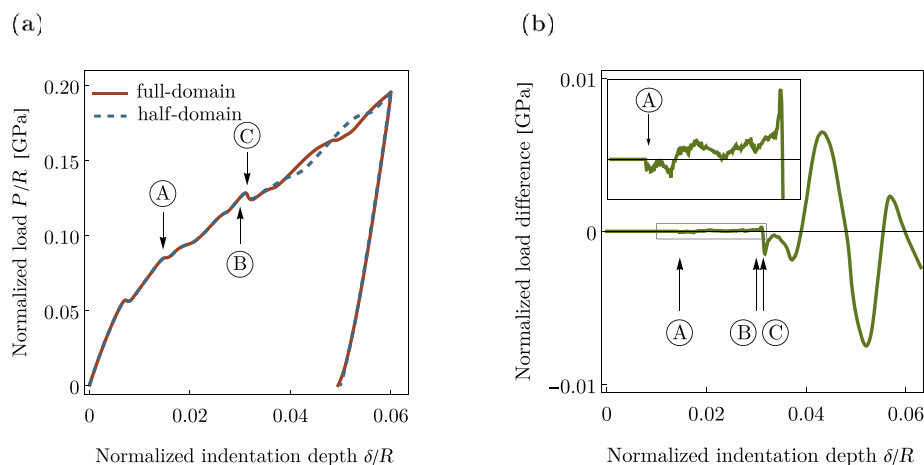


Fig. A.1. (a) Normalized indentation load–depth curves corresponding to the non-symmetric microstructure developed in the full domain and to the symmetric microstructure developed in the half domain. (b) The difference between the two loads (negative when the full-domain load is smaller than the half-domain load). The inset in panel (b) shows an enlarged part marked by a box.

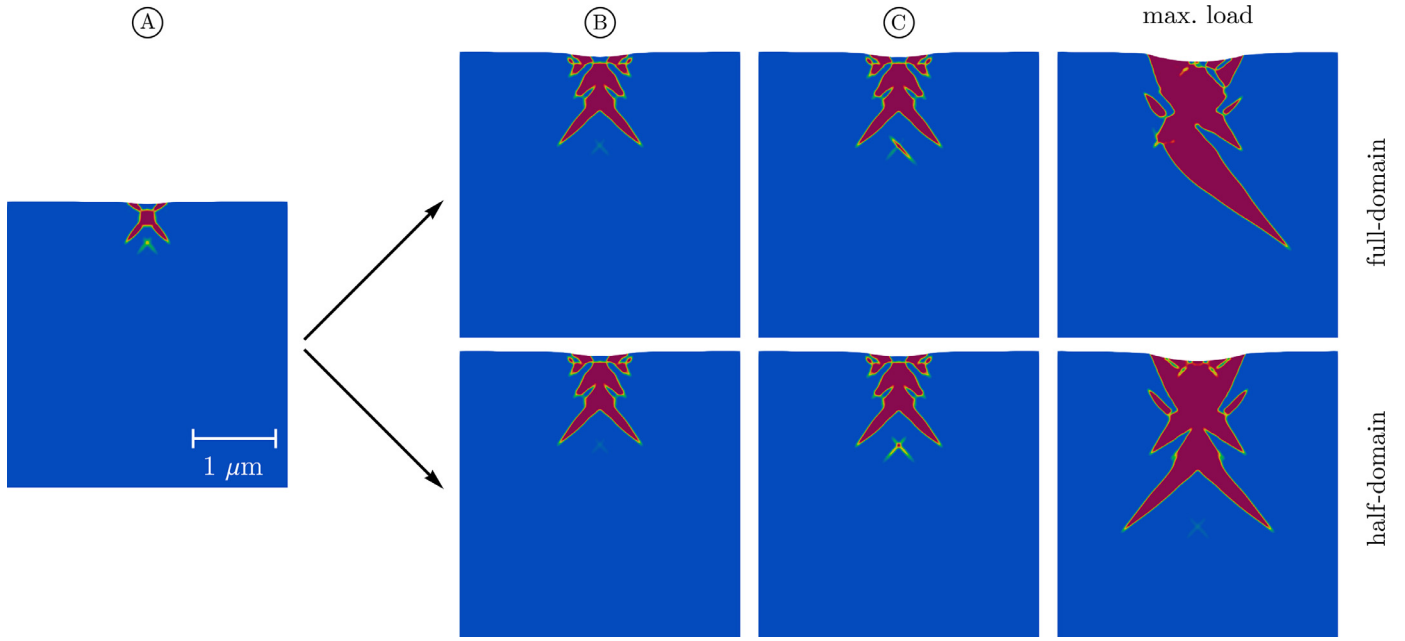


Fig. A.2. Comparison of the non-symmetric and symmetric microstructures developed, respectively, in the full domain and half domain. The instants A, B and C refer to Fig. A.1.

the microstructure is consistent with the small load difference between instants A and B.

A general observation from the simulations carried out within this work, including those not reported in the paper, is that the symmetry breakdown is hindered at smaller scales and for larger values of the interface thickness parameter  $\ell$ ,

i.e., for more diffuse interfaces. These observations are consistent with those reported in [55] in the case of phase-field modeling of martensitic transformation. As shown in [55], the indentation speed is an additional factor influencing propensity to symmetry breakdown (the lower the speed, the easier the breakdown); the related study is out of scope of this work.

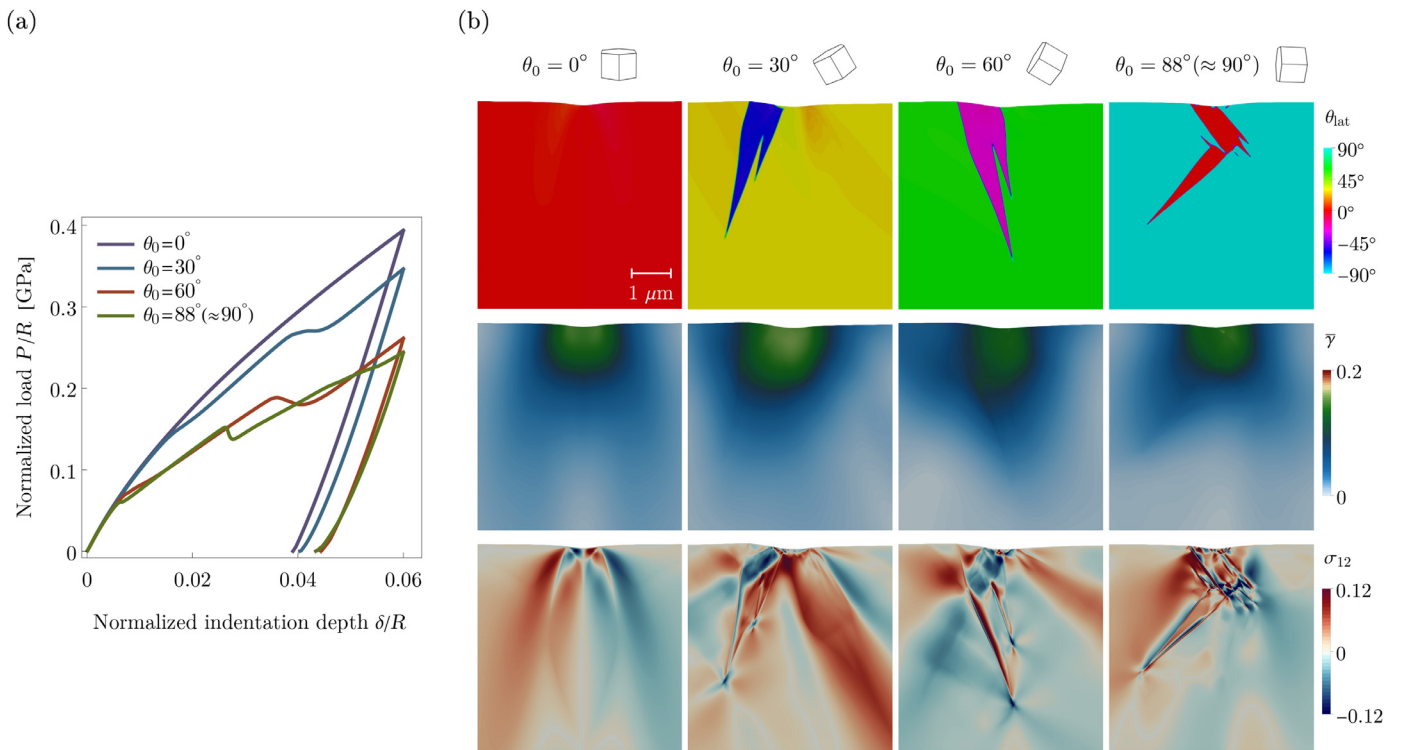


Fig. B.1. Effect of declination angle  $\theta_0$  on: (a) the indentation load–depth response, and (b) the microstructural features, as predicted by the model incorporating gradient plasticity effects. In panel (b), the first row depicts the lattice orientation angle  $\theta_{lat}$ , the second row depicts the plastic slip activity, and the third row depicts the shear stress distribution. The snapshots are taken at the fully-unloaded state.

## Appendix B. Indentation at different declination angles: gradient crystal plasticity

In this appendix, we provide additional results complementing the study of the effect of declination angle  $\theta_0$  reported in Section 3.3. The setup of the problem is identical to that in Section 3.3, except that the gradient-enhanced crystal plasticity model is used instead of the conventional one, see also Section 3.5. In particular, the same range of declination angles is analyzed for the indenter radius  $R = 2 \mu\text{m}$ . The results are summarized in Fig. B.1.

Qualitatively, the results are similar to those shown in Fig. 6. There is no twinning for  $\theta_0 = 0^\circ$ . The microstructures corresponding to the other declination angles show some differences, yet the orientations of lenticular-shaped twins appear to be consistent with those in the reference non-gradient plasticity simulations. The accumulated plastic slip  $\bar{\gamma}$  exhibits here a more spread-out distribution, an effect illustrated already in Fig. 13. As in the case of the conventional crystal plasticity, the case of  $\theta_0 = 0^\circ$  is characterized by the highest load, while the load is the lowest for  $\theta_0 = 60^\circ$  and  $\theta_0 \approx 90^\circ$ , see Fig. 7. At the same time, since the indenter radius ( $R = 2 \mu\text{m}$ ) is relatively small, the actual value of the indentation load is visibly affected by the gradient plasticity effects; the maximum load is here 15–25% higher depending on the declination angle, compare Figs. 6(a) and B.1(a).

## Supplementary material

Supplementary material associated with this article can be found, in the online version, at [10.1016/j.jma.2025.02.016](https://doi.org/10.1016/j.jma.2025.02.016)

## References

- [1] P.G. Partridge, *Metall. Rev.* 12 (1967) 169–194.
- [2] Reed-Hill, R. E., & Abbaschian, R. (1973). *Physical metallurgy principles*. Van Nostrand, 17
- [3] S. Mahajan, D.F. Williams, *Int. Metall. Rev.* 18 (1973) 43–61.
- [4] M.H. Yoo, *Metall. Trans. A* 12 (1981) 409–418.
- [5] M.H. Yoo, J.K. Lee, *Philos. Mag. A* 63 (1991) 987–1000.
- [6] T. Guo, F. Siska, M.R. Barnett, *Scr. Mater.* 110 (2016) 10–13.
- [7] T. Guo, F. Siska, J. Cheng, M. Barnett, *J. Alloys Compd.* 731 (2018) 620–630.
- [8] J. Cheng, T. Guo, M.R. Barnett, *J. Magn. Alloys* 10 (2022) 169–179.
- [9] G. Nayyeri, W.J. Poole, C.W. Sinclair, S. Zaefner, P.J. Konijnenberg, C. Zambaldi, *Mat. Sci. Engng. A* 670 (2016) 132–145.
- [10] D. Catoor, Y.F. Gao, J. Geng, M.J.N.V. Prasad, E.G. Herbert, K.S. Kumar, G.M. Pharr, E.P. George, *Acta Mater.* 61 (2013) 2953–2965.
- [11] R. Sánchez-Martín, M.T. Pérez-Prado, J. Segurado, J. Bohlen, I. Gutiérrez-Urrutia, J. Llorca, J.M. Molina-Aldareguia, *Acta Mater.* 71 (2014) 283–292.
- [12] C. Zambaldi, C. Zehnder, D. Raabe, *Acta Mater.* 91 (2015) 267–288.
- [13] R. Sánchez-Martín, M.T. Pérez-Prado, J. Segurado, J.M. Molina-Aldareguia, *Acta Mater.* 93 (2015) 114–128.
- [14] K.P. Raineesh, K.E. Prasad, *J. Mat. Res.* 37 (2022) 728–736.
- [15] H. Fan, S. Aubry, A. Arsenlis, J.A. El-Awady, *Scr. Mater.* 112 (2016) 50–53.
- [16] G. Nayyeri, W.J. Poole, C.W. Sinclair, S. Zaefner, *Scr. Mater.* 137 (2017) 119–122.
- [17] H. Kitahara, T. Mayama, K. Okumura, Y. Tadano, M. Tsushida, S. Ando, *Acta Mater.* 78 (2014) 290–300.
- [18] B.L. Wu, G.S. Duan, X.H. Du, L.H. Song, Y.D. Zhang, M.J. Philippe, C. Esling, *Mat. Des.* 132 (2017) 57–65.
- [19] Y.C. Lai, Y. Ying, D. Yadav, J. Guerrero, Y.J. Hu, K.Y. Xie, *J. Magn. Alloys* 11 (2023) 4513–4524.
- [20] H. Bei, Y.F. Gao, S. Shim, E.P. George, G.M. Pharr, *Phys. Rev. B* 77 (2008) 060103.
- [21] Y. Gao, H. Bei, *Prog. Mat. Sci.* 82 (2016) 118–150.
- [22] I.A. Alhafez, C.J. Ruestes, Y. Gao, H.M. Urbassek, *Nanotechnology* 27 (2015) 045706.
- [23] J. Varillas, J. Očenášek, J. Torner, J. Alcalá, *Acta Mater.* 217 (2021) 117122.
- [24] B. Selvarajou, J.H. Shin, T.K. Ha, I.S. Choi, S.P. Joshi, H.N. Han, *Acta Mater.* 81 (2014) 358–376.
- [25] F. Siska, T. Guo, L. Stratil, J. Cizek, M. Barnett, *Comp. Mater. Sci.* 126 (2017) 393–399.
- [26] S.M. Allen, J.W. Cahn, *Acta Metall.* 27 (1979) 1085–1095.
- [27] R. Kondo, Y. Tadano, K. Shizawa, *Comp. Mater. Sci.* 95 (2014) 672–683.
- [28] X. Hu, Y. Ji, L. Chen, R.A. Lebensohn, L.Q. Chen, X. Cui, *Int. J. Plast.* 143 (2021) 103019.
- [29] C. Liu, F. Roters, D. Raabe, *Acta Mater.* 242 (2023) 118444.
- [30] J. Hu, B. Xu, J. Xiong, C. Yu, G. Kang, *Int. J. Mech. Sci.* 284 (2024) 109734.
- [31] M. Rezaee-Hajidehi, P. Sadowski, S. Stupkiewicz, *J. Mech. Phys. Solids* 163 (2022) 104855.
- [32] N. Bruzy, C. Denoual, A. Vattré, *J. Mech. Phys. Solids* 166 (2022) 104921.
- [33] H. Liu, F.X. Lin, P. Zhao, N. Moelans, Y. Wang, J.F. Nie, *Acta Mater.* 153 (2018) 86–107.
- [34] P. Sadowski, M. Rezaee-Hajidehi, S. Stupkiewicz, *Comp. Mech.* (2024), doi:10.1007/s00466-024-02533-w.
- [35] K. Tůma, S. Stupkiewicz, H. Petryk, *J. Mech. Phys. Solids* 95 (2016) 284–307.
- [36] J.D. Clayton, J. Knap, *Physica D* 240 (2011) 841–858.
- [37] C. Liu, P. Shanthraj, M. Diehl, F. Roters, S. Dong, J. Dong, W. Ding, D. Raabe, *Int. J. Plast.* 106 (2018) 203–227.
- [38] S. Wulfinghoff, T. Böhlke, *Proc. Roy. Soc. A* 468 (2012) 2682–2703.
- [39] J.M. Scherer, V. Phalke, J. Besson, S. Forest, J. Hure, B. Tanguy, *Comp. Meth. Appl. Mech. Eng.* 372 (2020) 113426.
- [40] L.P. Evers, W.A.M. Brekelmans, M.G.D. Geers, *J. Mech. Phys. Solids* 52 (2004) 2379–2401.
- [41] M.E. Gurtin, L. Anand, S.P. Lele, *J. Mech. Phys. Solids* 55 (2007) 1853–1878.
- [42] C. Miehe, S. Mauthe, F.E. Hildebrand, *Comp. Meth. Appl. Mech. Eng.* 268 (2014) 735–762.
- [43] H. Petryk, S. Stupkiewicz, *Arch. Mech.* 68 (2016) 459–485.
- [44] T. Kaiser, A. Menzel, *J. Mech. Phys. Solids* 131 (2019) 276–302.
- [45] M. Ryś, S. Stupkiewicz, H. Petryk, *Int. J. Plast.* 156 (2022) 103355.
- [46] S. Forest, *J. Eng. Mech.* 135 (2009) 117–131.
- [47] C. Ling, S. Forest, J. Besson, B. Tanguy, F. Latourte, *Int. J. Solids Struct.* 134 (2018) 43–69.
- [48] P. Steinmann, E. Stein, *Comp. Meth. Appl. Mech. Eng.* 129 (1996) 235–254.
- [49] C. Miehe, *Int. J. Num. Meth. Engng.* 39 (1996) 3367–3390.
- [50] S. Stupkiewicz, H. Petryk, *Int. J. Num. Meth. Eng.* 93 (2013) 747–769.
- [51] P. Alart, A. Curnier, *Comp. Meth. Appl. Mech. Eng.* 92 (1991) 353–375.
- [52] J. Korelc, P. Wriggers, *Automation of Finite Element Methods*, Springer International Publishing, Switzerland, 2016.
- [53] K. Tůma, S. Stupkiewicz, H. Petryk, *J. Mech. Phys. Solids* 114 (2018) 117–142.
- [54] S.R. Kalidindi, *J. Mech. Phys. Solids* 46 (1998) 267–290.
- [55] M. Rezaee-Hajidehi, S. Stupkiewicz, *Mech. Mat.* 141 (2020) 103267.
- [56] H. Somekawa, T. Tsuru, A. Singh, S. Miura, C.A. Schuh, *Acta Mater.* 139 (2017) 21–29.
- [57] G. Nayyeri, W.J. Poole, C.W. Sinclair, S. Zaefner, *Scr. Mater.* 156 (2018) 37–41.
- [58] S. Gollapudi, M.A. Azeem, A. Tewari, U. Ramamurty, *Scr. Mater.* 64 (2011) 189–192.

- [59] R. Sánchez-Martín, C. Zambaldi, J.M. Molina-Aldareguia, M.T. Pérez-Prado, *Scr. Mater.* 104 (2015) 9–12.
- [60] G.M. Pharr, E.G. Herbert, Y. Gao, *Ann. Rev. Mat. Res.* 40 (2010) 271–292.
- [61] W.D. Nix, H. Gao, *J. Mech. Phys. Solids* 46 (1998) 411–425.
- [62] Q. Yu, Z.W. Shan, J. Li, X. Huang, L. Xiao, J. Sun, E. Ma, *Nature* 463 (2010) 335–338.
- [63] K.E. Prasad, K. Rajesh, U. Ramamurty, *Acta Mater.* 65 (2014) 316–325.